

**Nellie: Automated organelle segmentation, tracking,
and hierarchical feature extraction in 2D/3D live-cell microscopy**

Austin E. Y. T. Lefebvre^{1,*}, Gabriel Sturm^{1,2}, Ting-Yu Lin¹, Emily Stoops¹, Magdalena Preciado López¹, Benjamin Kaufmann-Malaga¹, Kayley Hake¹

¹Calico Life Sciences LLC, South San Francisco, CA, 94080

²Department of Biochemistry and Biophysics, University of California San Francisco,
San Francisco, CA, 94158

*Address correspondence to

Austin E. Y. T. Lefebvre, Ph.D.
Calico Life Sciences
1170 Veterans Blvd
South San Francisco, CA, 94080
Email: austin.e.lefebvre+nellie@gmail.com

Abstract

The analysis of dynamic organelles remains a formidable challenge, though key to understanding biological processes. We introduce Nellie, an automated and unbiased pipeline for segmentation, tracking, and feature extraction of diverse intracellular structures. Nellie adapts to image metadata, eliminating user input. Nellie's preprocessing pipeline enhances structural contrast on multiple intracellular scales allowing for robust hierarchical segmentation of sub-organellar regions. Internal motion capture markers are generated and tracked via a radius-adaptive pattern matching scheme, and used as guides for sub-voxel flow interpolation. Nellie extracts a plethora of features at multiple hierarchical levels for deep and customizable analysis. Nellie features a Napari-based GUI that allows for code-free operation and visualization, while its modular open-source codebase invites customization by experienced users. We demonstrate Nellie's wide variety of use cases with two examples: unmixing multiple organelles from a single channel using feature-based classification and training an unsupervised graph autoencoder on mitochondrial multi-mesh graphs to quantify latent space embedding changes following ionomycin treatment.

Main

The complex weave and elaborate dance of organelles lies at the center of cellular physiology and pathology. For example, the alterations and balance of mitochondrial dynamics coregulate its turnover, quality control, mtDNA organization, and bioenergetic output^{1–5}. Importantly, organelles can also form contact sites between one another, allowing for the exchange of metabolites, ions, and proteins, and promote autophagic turnover, where dysfunctions in any of these have been correlated with aging and other various diseases^{6–9}. The topic of organelles as drivers of physiological dysfunction is clearly important; however, the dynamic morphology and motility of these organelles, coupled with limitations inherent to microscopy such as acquisition speed, the diffraction limit, and tradeoffs between signal and phototoxicity, pose significant challenges in extracting this information. This results in manually involved or organelle-specific pipelines that do not generalize well to broader datasets. Consequently, there is a pressing need for a widely accessible analytical tool capable of providing detailed extraction of spatial and temporal features at multiple organellar scales, but that remains independent of the tool's user or the organelle in question.

Many tools exist for intracellular structural segmentation and tracking^{10–28}. However, the pipelines either rely heavily on manual or semi-automated techniques, which are time-consuming, prone to subjective bias, and often infeasible for large and/or spatially 3D datasets. Automated methods, which offer improvements in speed and objectivity, frequently struggle with the complexity and variability inherent in biological imaging data. Common issues of existing tools include the inability to effectively handle

multi-scale structures present between or even within datasets, insufficient segmentation accuracy for dim or small objects, and limitations in tracking algorithms, particularly in dense and dynamically complex cellular environments. Additionally, most tools rely on the assumption that an organelle is a single and temporally consistent entity with only occasional and specifically defined merging or splitting events, which limits the quantification of these phenomena to arbitrary metrics. Recent clever uses in advanced image processing and machine learning techniques have begun to address these challenges^{10,14,28–30}. However, there remains a significant gap in the development of a comprehensive, automated, and organelle-agnostic pipeline capable of efficiently and accurately processing large-scale and multi-dimensional microscopy datasets.

In this paper, we introduce Nellie, short for organellometer, a novel image analysis pipeline designed specifically to address these challenges. By incorporating multi-scale structure-enhancing preprocessing methods, Nellie is able to segment and hierarchically divide organelles into logical subcomponents. These subcomponents are interrogated to produce motion capture markers that are compared via local, variable-range feature and pattern matching to create linkages between adjacent frames. These linkages act as beacons for novel temporal interpolation algorithms to provide sub-voxel tracking capabilities. We incorporate and introduce a multitude of both standard and advanced quantification techniques to extract a hierarchical pool of descriptive multi-level spatial and temporal features to choose from. The whole pipeline can be run on CPU or accelerated via GPU, and its outputs are made easily accessible via a Napari plugin (Extended Data Fig. 1)

To showcase the broad range of potential uses that Nellie and its extracted features offer, we present two use cases that we hope will serve to inspire more advanced developments on Nellie's extracted features. First, we show how one can use Nellie's outputs to unmix multiple organelle types from a single channel of a fluorescence timelapse. Second, using Nellie's outputs we develop a novel multi-mesh approach to organelle graph construction, inspired by DeepMind's recent GraphCast paper³¹. We use this multi-mesh to train an unsupervised graph autoencoder, and use the model to compare mitochondrial networks across a complex feature-space. We hope that this work not only provides a valuable tool for cellular biologists but that it also sets a new standard for automated image analysis as a whole.

Results

Multi-scale adaptive filters enhances structural features of organelles

Nellie accepts multi-dimensional image data, anything from 2D (YX) to 5D (CTZYX), of fluorescently labeled organelles as inputs (Fig. 1a). Laser and dye properties can cause the signal-to-noise of organelles to fluctuate widely both between and within datasets. In the preprocessing stage of our pipeline, a multi-scale modified Frangi filter is implemented to enhance the inherent structural contrast of organelles, allowing for segmentation based on local structure rather than fluorescence intensity (Fig. 1b)³². Our filter is empirically optimized for structures in the size range of typical organelles, and automatically adjusts the filter's effective range based on voxel dimensions to adapt to various magnifications and anisotropies. This is followed by an adaptive Frangi filter parameter calculation on a scale-by-scale basis to enhance structures of multiple sizes (Supplementary Note 1). Our pipeline contrasts with the current state-of-the-art of traditional intracellular segmentation pipelines, which are not adaptive to intrinsic image metadata, and if included, use the same filter parameters across all scales of structural enhancement, limiting the robustness of the filter and subsequent segmentation of variable-scale objects^{12,14}.

For each scale, several steps are undertaken. First, the gamma parameter for the Frangi filter is derived from the minimum of the triangle and Otsu threshold values – termed henceforth as the Minotri threshold – of the Gaussian filtered image, providing a size-adaptive approach to contrast enhancement of structural features (Supplementary Note 2)^{33,34}. Next, the Hessian matrix for each sigma level is computed and

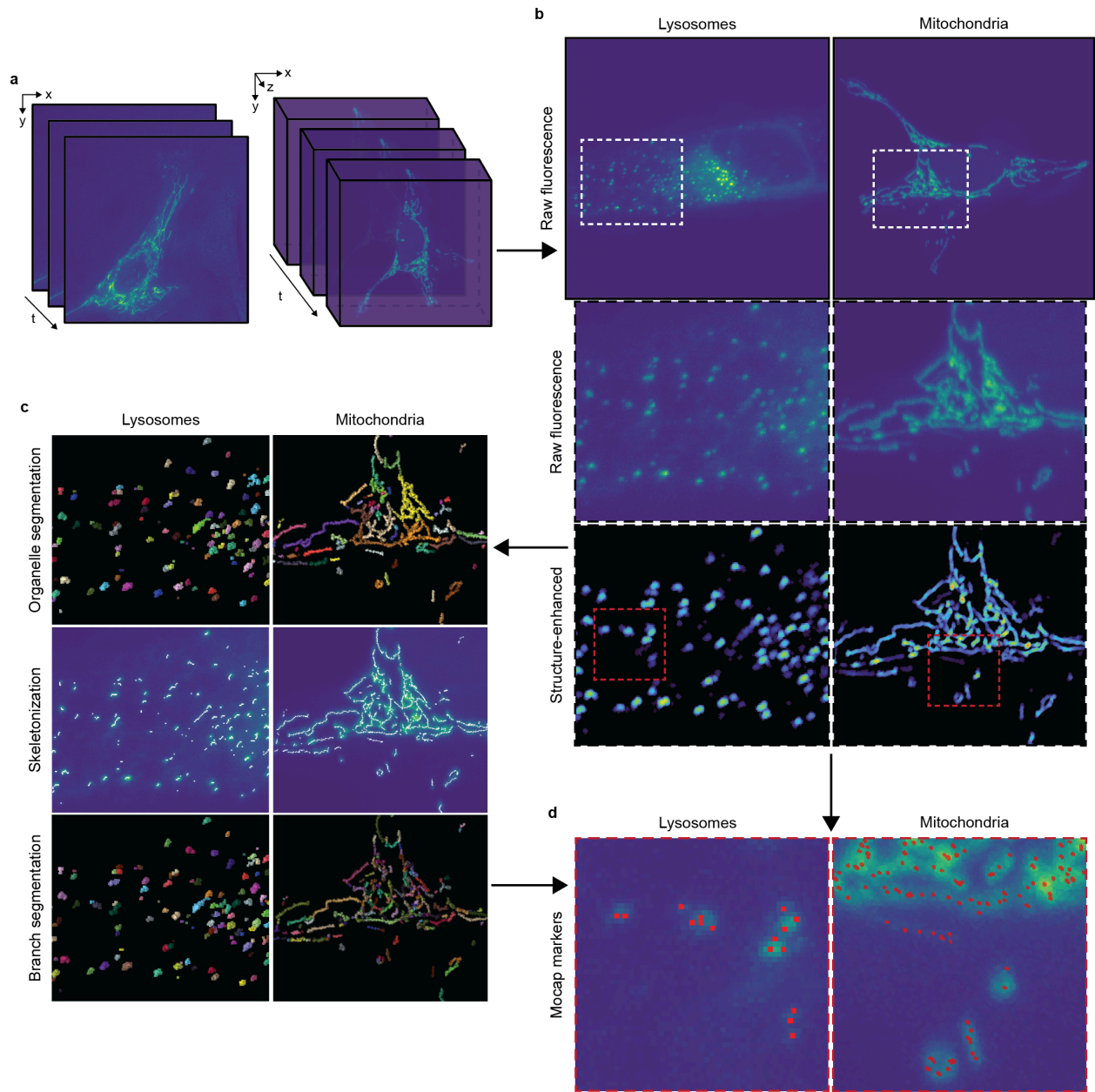


Fig. 1: Automated multi-scale preprocessing, hierarchical segmentation, and motion capture marking of organelles in 2D and 3D live-cell images.

a, A 2D or 3D temporal stack of fluorescently labeled organelles is used as input to Nellie. **b**, Nellie performs structural contrast enhancement on a wide variety of diverse organelles, such as spherical lysosomes (left) and elaborate networks of mitochondria (right) via multiple multi-scale filtering algorithms. **c**, Instance segmentation separates objects by connected pixels (top), while skeletonization of the segmentations (middle) allows for branch-based subcompartment segmentation within connected components (bottom), resulting in little change in spherical structures such as lysosomes (left), but adding hierarchies in networked structures like mitochondria (right). **d**, Motion capture markers are automatically detected via multi-scale local max peak detection in lysosomes (left) and mitochondria (right) using information from the structure-enhanced image, and constrained within the semantic segmentation mask for use in downstream temporal linkages. All reference images (**b-d**) are of 3D (ZYX) volumes.

subsequently masked at that specific scale using the Minotri threshold of the Frobenius norm of the rescaled Hessian matrix, a modified approach to MitoGraph's masking method³⁵. This approach not only significantly improves computational and memory efficiency, which is particularly crucial for eigenvalue calculations of large datasets, but also allows for completely automatic parameter selection. The eigenvalues of the vectorized Hessian matrix are calculated in memory-efficient chunks and sorted by their absolute values within individual voxels. Finally, Frangi dissimilarity metrics are calculated from shape-balanced alpha and beta values and the scale-adaptive gamma value (Extended Data Fig. 2, Supplementary Note 3). These metrics are then used to calculate the inherent structural measure of the organelles at that specific scale, rather than the traditional approach of using the same metrics across all scales. The final multi-scale structure-enhanced filtered image – termed henceforth as the preprocessed image – is constructed by compiling the maximum voxel-wise value across all Frangi filter scales, ensuring that the most prominent features at each scale are captured in the final image (Fig. 1b, Extended Data Fig. 3, Supplementary Note 4).

Hierarchical deconstruction allows for multi-level organelle instance segmentation

Before answering how an organelle changes, we must first ask ourselves how an organelle should be represented. Individual organelles are rarely ever individual organelles at all, but rather belong to a complex and continuously evolving organellar landscape. In this regard, it is useful to instead think of and represent organelles as a hierarchical collection of objects at independent frames; the organellar landscape of a

cell at a single frame is made up of spatially disconnected organelles, which is in turn made up of numerous subcompartments, which can be broken down into nodes, voxels, or even sub-voxel regions. To capture this representation, Nellie performs several steps to deconstruct our organellar landscape. First, we employ the Minotri threshold on the preprocessed image generating a semantic segmentation mask - our organellar landscape. In the case of 3D images, a binary hole-filling algorithm is applied to address any internal inconsistencies within the segmented organelles (Supplementary Note 5). Following thresholding, a binary opening operation is conducted to smooth out noisy or irregular boundaries of the organelles and enhance the accuracy of the subsequent segmentation by removing weak, single-voxel connections (Extended Data Fig. 4). We then perform a simple connected-components based labeling scheme to generate instance segmentations of individual objects - our spatially disconnected organelles (Fig. 1c). We then use an octree-based (or quadtree in 2D) skeletonization to reduce the semantic segmentation masks to single-voxel wide representations (Fig. 1c)^{36,37}. The skeleton representation is used to identify network junction nodes (branching points) within individual components, which allows us to deconstruct the organelle network into individually labeled branches - our organelle subcompartments (Fig. 1c). We further break down these subcompartments into individual skeleton nodes, which hold properties of their radius-dependent surrounding voxels. To maintain a continuous linkage across all levels of our hierarchy, we can generate adjacency maps by iteratively reassigning the semantic segmentation mask voxels via a k-dimensional (k-d) tree of the skeleton nodes and their branch labels, enabling the graph-like traversal of our organellar landscape between any hierarchical level³⁸.

Motion capture markers are generated for downstream tracking

The consistency of segmentations and skeleton networks are notoriously finicky between timepoints, which causes linkage problems when using center-of-mass or skeleton-based tracking approaches. To avoid these problems, we instead generate motion capture (mocap) markers within our organelles, completely independently of our labels, and use these as a basis for linking variable-radius regions of our image across timeframes. This is in line with representing the organellar landscape as a dynamic entity, rather than tracking specific instance segmentations. To do this, Nellie performs a computationally efficient distance transformation over our semantic segmentation mask³⁹ (Extended Data Fig. 5, Supplementary Note 6). Next, a multi-scale and adaptive local maxima peak detection scheme is employed (Supplementary Note 7). To do this, the distance-transformed image is filtered using a Laplacian of Gaussian (LoG) filter with the same set of scales as in the preprocessing pipeline (Extended Data Fig. 6). A maximum filter is then applied across the multi-scale LoG filtered images (Extended Data Fig. 6). Voxels in the maximum filtered volume that match the voxels in the corresponding volume slice of the LoG filtered image are classified as local maxima, or peaks, for that particular scale (Extended Data Fig. 6). The stack of local maxima images is flattened, and the peaks are used as our mocap markers (Fig. 1d).

Features for each motion capture marker are gathered via variable-range queries

To temporally link these mocap markers, a comprehensive feature vector is constructed to encapsulate critical aspects of the organelles' local characteristics and dynamics. At

each mocap marker, the distance transformed value, representing the organelle's radius at that point, is multiplied by two, providing the dimensions for the bounding box of each marker (Fig. 2a). Within these bounding boxes, the mean and variance are computed for both the raw image and the preprocessed image. These statistics are collectively termed as the 'stats vector' (Fig. 2b). Furthermore, the first six 2D Hu moment invariants of the raw intensity image and the preprocessed image within the mocap marker's bounding box regions are computed to generate translation, scale, and rotation invariant comparison metrics⁴⁰. In 3D, these 2D Hu moment invariants are calculated for xy, xz, and yz projections of the 3D bounding box region, resulting in what we term as the 'Hu vectors' (Fig. 2c). To link markers between adjacent frames, a multi-faceted cost matrix is constructed. First, a speed matrix is created by calculating the displacement between all marker indices in adjacent frames (t and $t+1$) and dividing this by the corresponding time between frames. The speeds are normalized to the maximum permissible speed, defaulting to 1 $\mu\text{m}/\text{sec}$. Any linkages exceeding the maximum distance threshold are prohibited. The distance matrix is then z-score normalized for standardization. Absolute value differences of the stats vectors for markers between the two frames are computed and standardized. The resulting matrix is divided by the number of feature columns in the stats vector to provide balanced weighting in the final cost matrix. Absolute value differences of the Hu vectors for markers between the two frames are computed and standardized. The Hu matrix, after normalization, is adjusted by dividing the matrix by the number of feature columns in the Hu vector, which varies depending on whether the dataset is 2D or 3D. The standardized distance, stats, and Hu matrices are summed to form the final cost matrix, which will be used to temporally link mocap markers (Fig. 2d).

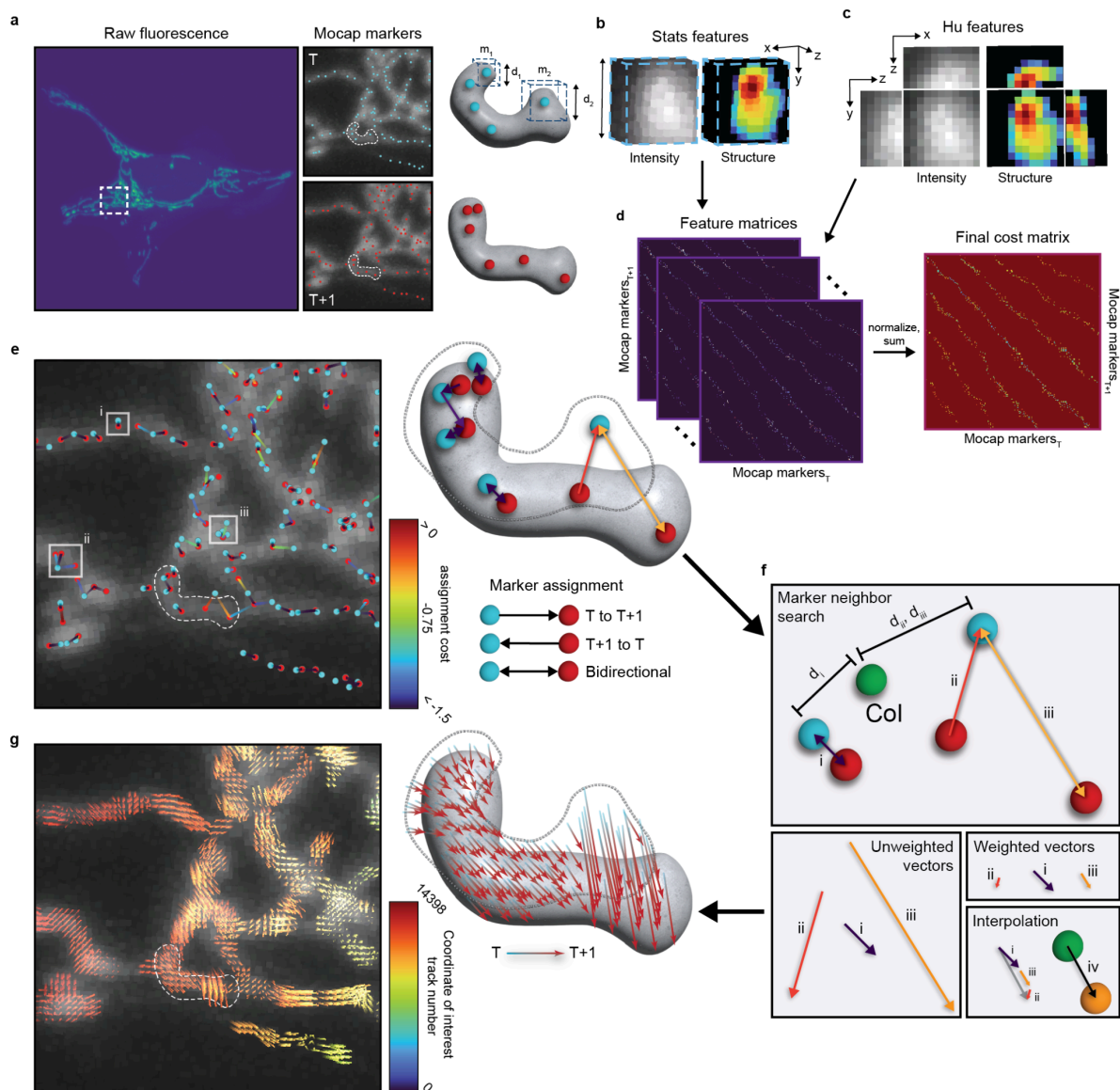


Fig. 2: Linking motion capture markers and interpolating sub-voxel movements of organelles.

a, Fluorescently labeled mitochondria (left) and their respective mocap markers for time T (top right, blue dots) and T+1 (bottom right, red dots). Feature search bounding boxes are marked by dotted lines for two mocap markers (m_1 , m_2) with different radii (d_1 , d_2) at time T. **b**, 3D search bounding box raw intensity values (left) and post-structural enhancement values (right) of m_2 , which are used for calculating stats features. **c**, 2d orthogonal max projections in xy, xz, and yz of raw intensity values (left) and post-structural enhancement (right) of mocap marker 2, which are used for calculating Hu features. **d**, Difference matrices of distance, Hu features, and stats features are calculated between mocap markers in frame T (columns) and T+1 (rows) to create weighted feature matrices (left), which are then z-score normalized and summed to create the final cost matrix for marker linkage (right). **e**, Mocap markers from frame T (blue dots) are linked to their best mocap marker match in T+1 (red dots) based on assignment cost (line colors), and vice-versa for T+1 to T, resulting in 1-to-1 (i), 1-to-N (ii), or N-to-1 (iii) matches. **f**, A coordinate of interest (Col, green sphere) not corresponding to a mocap marker (red, blue spheres) has a flow vector interpolated via distance-weighted and cost-weighted vector summation of nearby assigned mocap marker linkages to a new coordinate at T+1 (orange sphere). **g**, Interpolated flow vectors for all voxels in the image (left) and flow vector representations (arrows) for all voxels within a mitochondrion (right) between time T (blue) and T+1 (red).

Motion capture markers are tracked and used as guides for sub-voxel flow interpolation

Rather than solving the linear assignment problem by minimizing the global cost of mocap marker linkages, markers from frame t are simply assigned to their best-matched markers in frame $t+1$ and vice versa, allowing for 1-to-1 matching, 1-to-N matching, and N-to-1 matching (Fig. 2e). Each assignment results in a vector pointing from a marker at time t to another marker at $t+1$, and vice versa, with an associated cost to that linkage. It is important to emphasize that these motion capture markers and their linkages do not represent the final organelle tracks but rather serve as the beacons that point in the direction of local motion to inform the subsequent sub-voxel flow interpolations that serve as tracks. Once markers are assigned, any arbitrary coordinate or coordinates of interest (Col) can have its flow vector interpolated, meaning the motion of an entire organellar object's collection of voxels, or a single branch's collection of voxels, or even a single voxel or sub-voxel point within an organelle can be interrogated.

For interpolating flow vectors of Cols forwards in time from frame t , a k-d tree is first constructed using the coordinates of markers at frame t , facilitating efficient nearest-neighbor searches. All nearby marker coordinates within the maximum travel distance from the Col are then identified, and the distances between these detected markers and the Col are calculated by querying the k-d tree. Each detected marker's flow vector for interpolation of the Col's flow vector is weighted based on a preference for vectors that are closer and have a lower assignment cost value, indicating a better match during mocap marker linkage. The final interpolated vector from frame t to $t+1$ is

the sum of these weighted vectors (Fig. 2f). A similar process for markers at frame $t-1$ to frame t is performed for interpolation of flow vectors backwards in time. This interpolation process is efficiently executed in parallel for all Cols, resulting in a list of flow vectors that represent the interpolated motion of the Cols to the adjacent frame (Fig. 2g).

Remarkably, these flow vectors can be used to match voxels between timepoints, meaning one can determine the fate of each individual voxel coming from an organelle, or any part of its segmentation hierarchy, across all frames of a timelapse (Extended Data Fig. 7, Supplementary Note 8). Additionally, we note that this novel tracking and interpolation method is not limited to organelles or fluorescence microscopy and can easily be adapted to other types of images, including those segmented via, for example, Meta's Segment Anything Model (Extended Data Fig. 8)⁴¹.

Organellar features are calculated at and between multiple hierarchical levels

Though segmentation and tracking of organelles is useful for data exploration and visualization, objective interpretation only becomes possible when quantifiable features are available. To this end, Nellie allows for the calculation and export of a plethora of features specific to each level of the segmentation hierarchy, as well as the statistical investigation of inter-level features, such as an organelle's mean branch feature values, or a branch's nodes' mean feature values, etc (Supplementary Table 1).

Nellie begins with the calculation of features at the single-voxel level, such as fluorescence and structural intensity values from the raw and preprocessed images (Fig. 3a). Using the mocap marker linkages, flow vectors are interpolated for each voxel in the semantic segmentation mask, allowing for the extraction of features such as angular and linear velocity and acceleration, and directionality of each voxel with respect to its branch's pivot point (defined as the voxel within a branch that has the smallest velocity vector magnitude between the two frames of interest) or the image's center of mass, at each individual voxel (Fig. 3a, Supplementary Note 9).

Next, at the single-node level, which are centered around individual skeleton voxels, Nellie calculates the thickness of the organelle at that node, the divergence, convergence, and vergence (sum of the two) of its corresponding voxels' flow vectors to the node center, as well as linear and angular magnitude and orientation flow vector variability metrics (Fig. 3b, Extended Data Fig. 9, Supplementary Note 9).

At the single-branch level, Nellie calculates skeleton-specific features, such as the length, thickness, aspect ratio, and tortuosity of the branch's skeleton, but also features such as the branch's corresponding segmentation mask's area, major and minor axis length, extent, and solidity (Fig. 3c, Supplementary Note 9).

Finally, at the single-organelle level, Nellie calculates standard region properties, such as the area of the organelle, its major and minor axis length, its extent, and its solidity (Fig. 3d).

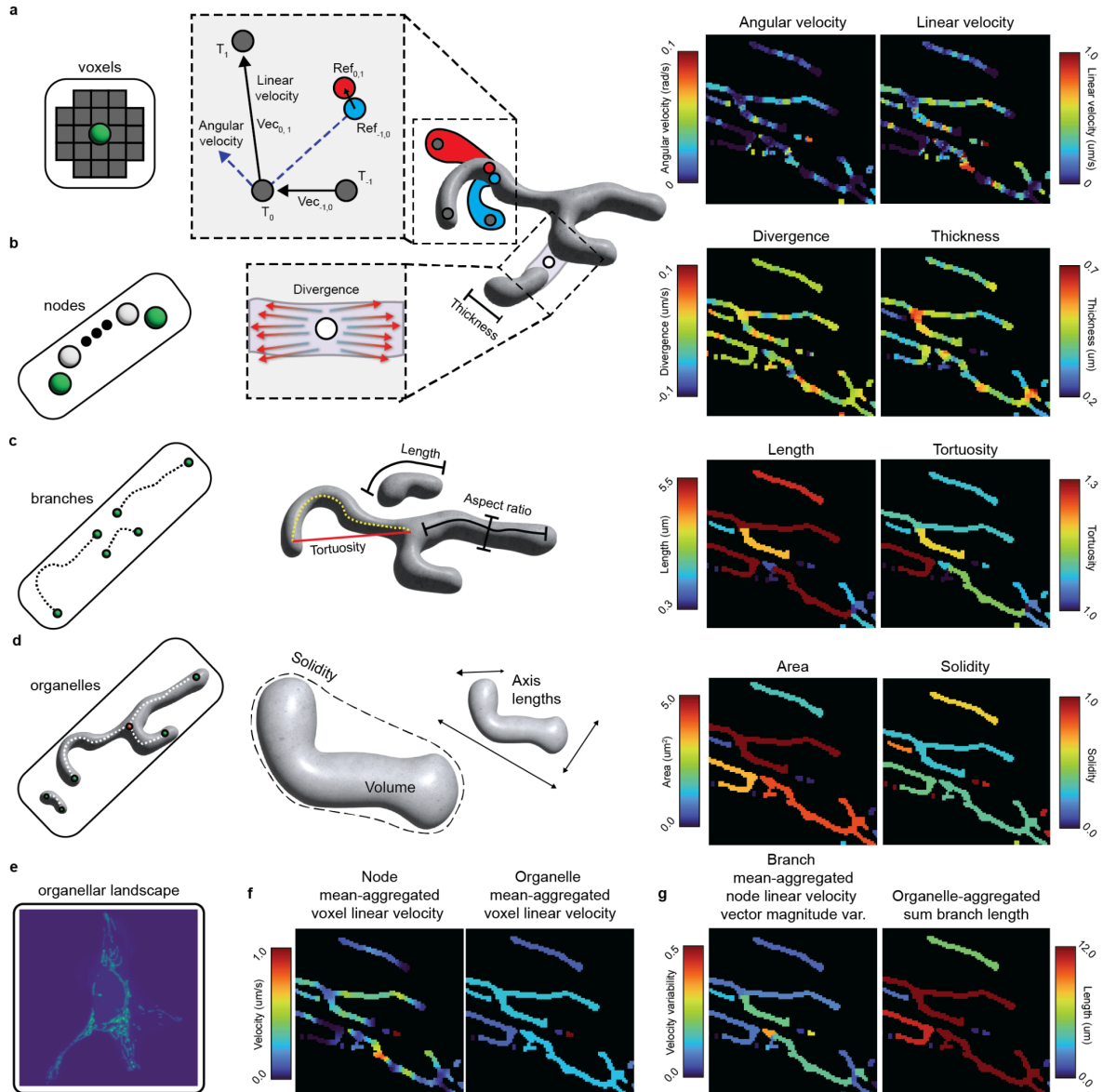


Fig. 3: Extraction of spatial and temporal features of organelles at multiple hierarchical levels.

a. Individual voxels represent the lowest hierarchical resolution of our organelle, containing feature information such as voxel intensities and motility metrics. Shown here is a subset of motility features extracted for one tracked voxel (gray dots) through time $T-1$ (blue structure) to $T+1$ (red structure). The tracked reference point for each time point (blue dot, red dot) is shown, and is used to calculate reference-adjusted linear and angular movements. **b.** Individual skeleton nodes represent the next level of the organellar hierarchy, encapsulating voxels within a radius corresponding to that node's border distance, containing features such as divergence / convergence of surrounding flow vectors, thickness, and more. **c.** Individual branches represent the next level of the organellar hierarchy, containing information on the curviness (tortuosity), length, aspect ratio, and more. **d.** Organelles represent the next level of the organellar hierarchy, spatially disconnected components in the image, containing information about volume, solidity, axis lengths, and more. **e.** The organellar landscape as a whole represents the highest level of our hierarchy, containing aggregate information from all levels below it. **f.** Each hierarchical level can aggregate metrics from its lower level's components, such as a node's or organelle's voxels' mean linear velocity. **g.** Other metrics as complex as a branch's nodes' mean linear velocity vector magnitude variability, or as simple as an organelle's branches' sum branch length can be calculated as well. All images were color-mapped via Nellie's Napari plugin.

For all of these metrics, Nellie also outputs a final aggregate dataset, allowing for interpretation of image-wide averages, maximum values, minimum values, variability, etc or the entire organellar landscape (Fig. 3e). Nellie also calculates statistics of aggregate values for features calculated at lower hierarchical levels. For example, a mean aggregation of linear velocities coming from voxels within a node or organelle can be calculated for each node and organelle as a whole (Fig. 3f). A variety of aggregation metrics can be calculated, from those as complex as a branch's nodes' mean linear velocity vector magnitude variability, to those as simple as summing the lengths of all the branches within an organelle connected component (Fig. 3g). The values for each of these level-specific and aggregated features can additionally be overlaid as a colormap for each voxel, node, branch, or organelle label, and viewed with the features' corresponding histogram in Nellie's Napari plugin, allowing for easy data exploration and visualization (Extended Data Fig. 1).

Case Study 1: Nellie's extensive feature quantification allows for unmixing of multiple organelle types in a single channel

In cellular microscopy, imaging more than a few organelle types in live cells within a single time series is a formidable challenge, often constrained by the limited availability of imaging channels, dye or fluorophore specificity, and the necessity to minimize phototoxicity and photobleaching. We introduce an innovative methodology that synergizes the advanced feature extraction capabilities of our pipeline, Nellie, with machine learning classification techniques. This approach enables the *post-hoc*

differentiation of organelles in single-channel images, effectively addressing a critical bottleneck in cellular imaging.

Utilizing multi-channel timelapse fluorescence microscopy, we separately captured images of Golgi apparatus and mitochondria (Fig. 4a). These independent channels were processed through Nellie to extract organelle-specific features. For validation, we generated combined organelle images, comprising both mitochondria and Golgi in a single channel, from the maximum intensity channel-projections of the two channels, and ran this projection image through Nellie to generate instance segmentations and extract their corresponding spatial and temporal features (Fig. 4b). To establish ground truth for the combined channel timelapse, we quantified the overlap of mask voxels between the multi-channel and the combined-channel masks. Organelles were labeled as mitochondria or Golgi based on the predominant overlapping channel.

Employing the multi-channel features from Nellie, we developed three Random Forest classifier models, each trained on either motility features alone, morphology features alone, or a combination of both⁴². The selection of features was grounded both empirically and through the analysis of features showing the most significant fold differences between mitochondria and Golgi (Fig. 4c). We intentionally exclude voxel intensity metrics in the models as intensity is not inherently dependent on structure. The models' efficacies were tested by comparing the models' predicted organelle types to the ground truth organelle types. We captured timelapses of 11 cells and used each cell in an 11-fold leave-one-out cross-validation, leaving one timelapse out of the training set

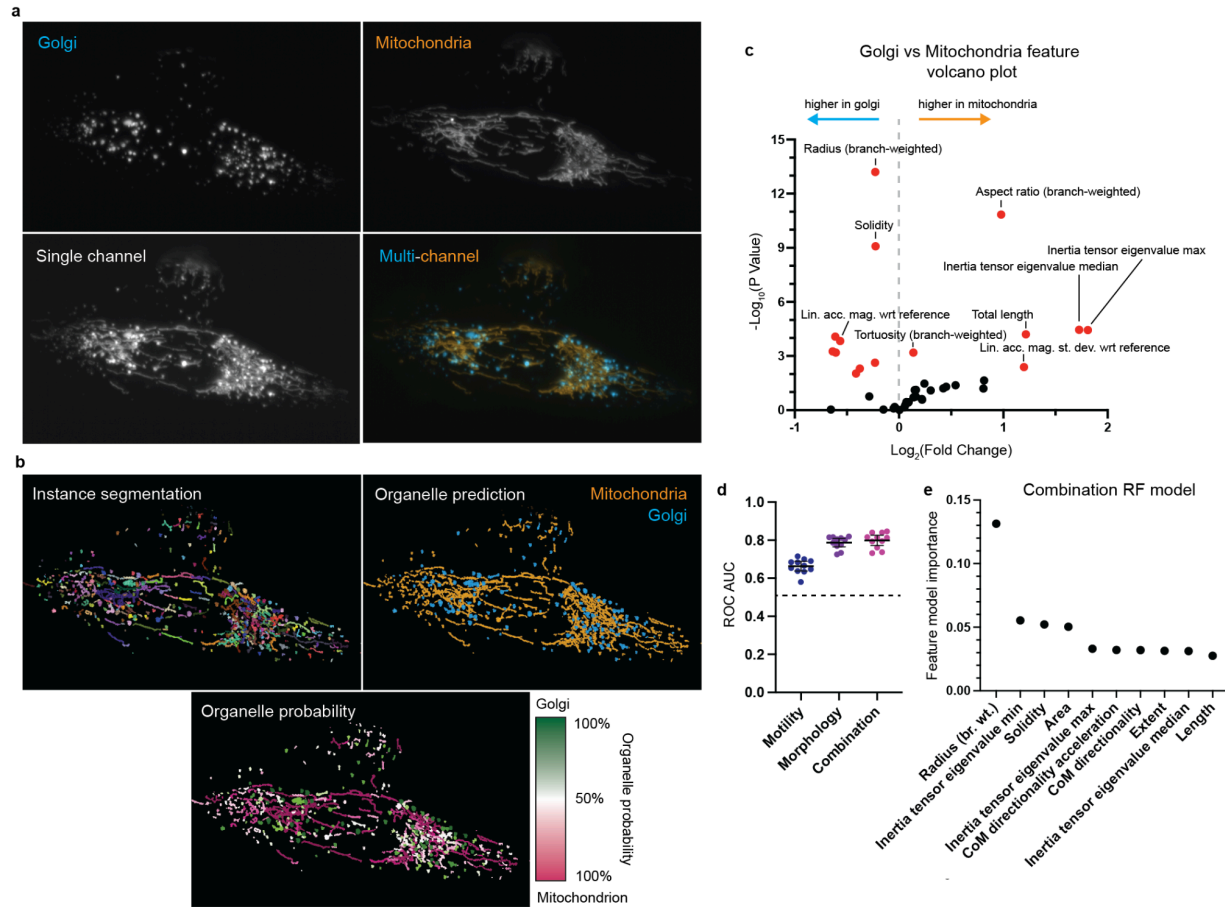


Fig. 4: Single-channel multi-organelle unmixing using features extracted by Nellie.

a. Raw intensity images of fluorescently labeled Golgi and mitochondria (top). A single channel max-intensity projection (bottom left) over the channel dimension, combining the fluorescence signal from both channels (bottom right) into one. **b.** The branch-based instance segmentation output derived from Nellie of the single channel image (top left). The binary organelle prediction from a trained random forest classifier (top right) and their corresponding probabilities (bottom). **c.** A volcano plot showing features upregulated (positive) or downregulated (negative) in mitochondria compared to Golgi, with significantly different ($p < 0.05$) features colored in red. **d.** Areas under the receiver operating characteristic curve for $N=11$ leave-one-out random forest classifier models with only motility features, only morphology features, or a combination of both. Bars are mean \pm standard deviation. **e.** Random forest model feature-importance for the classification of the representative image's organelles.

for testing for each cross-validation to evaluate each model, reflecting a realistic experimental scenario with limited sample sizes. Our validation results were promising, with all models surpassing the 0.50 threshold indicative of random guessing in the area under the curve (AUC) of the receiver operating characteristic curve (ROC). The combined model achieved an average AUC of 0.80, followed by 0.79 for morphology-only features, and 0.66 for motility-only features (Fig. 4d). Additional performance metrics also follow similar trends (Extended Data Fig. 10). Moreover, the model allowed us to identify the most impactful features contributing to its performance. These features include a higher aspect ratio and length in mitochondria, owing to its more networked morphology, and a larger radius and solidity in golgi, due to its more spherical shape (Fig. 4e).

This study demonstrates the potential of Nellie in advancing cellular organelle microscopy, especially under conventional imaging constraints. Leveraging standard random forest classification models from features extracted by Nellie, our method adeptly distinguishes complex biological structures in single-channel images, creating a significantly useful tool in the field of cellular imaging.

Case Study 2: Nellie's hierarchical organelle segmentation allows for the learning of comparable variable-range latent space representations of organelle graphs

In cellular microscopy, the intricate task of analyzing organelle networks demands innovative approaches, particularly when examining dynamic alterations in organelle organization. Here, we introduce a groundbreaking method that employs graph-based

latent space representations to interpret changes in organellar networks. By transforming skeletonized networks of organelle segmentation masks into graph structures and utilizing a graph autoencoder to transform Nellie's extensive feature outputs into a comparable representation, we decode subtle shifts in organellar arrangements.

We first define the nodes of our graph as skeleton voxels underlying the organelle segmentation masks, with each node encapsulating features of the adjacent organelle voxels. Utilizing the distance-transformed image, we determine the radius representative of each node. The features of surrounding voxels within this radius and the semantic segmentation mask—including raw intensity, structural enhancement, and motility features—are aggregated to form a comprehensive feature set for each node.

Inspired by DeepMind's GraphCast multi-mesh, our method constructs a multi-level graph network to efficiently facilitate message passing at multiple distances within the organelle graph³¹. Intuitively, this graph represents intra-organellar feature dependence, where each node depends, in part, on all other nodes' features within the organelle. The adjacency matrix's construction begins with the selection of a tip node, connecting nodes at increasing powers of two to establish a multi-level mesh (Fig. 5a, Supplementary Note 10).

The graph autoencoder architecture is pivotal in our methodology (Fig. 5b, Supplementary Note 11)⁴³. We use an initial multilayer perceptron (MLP) to transform

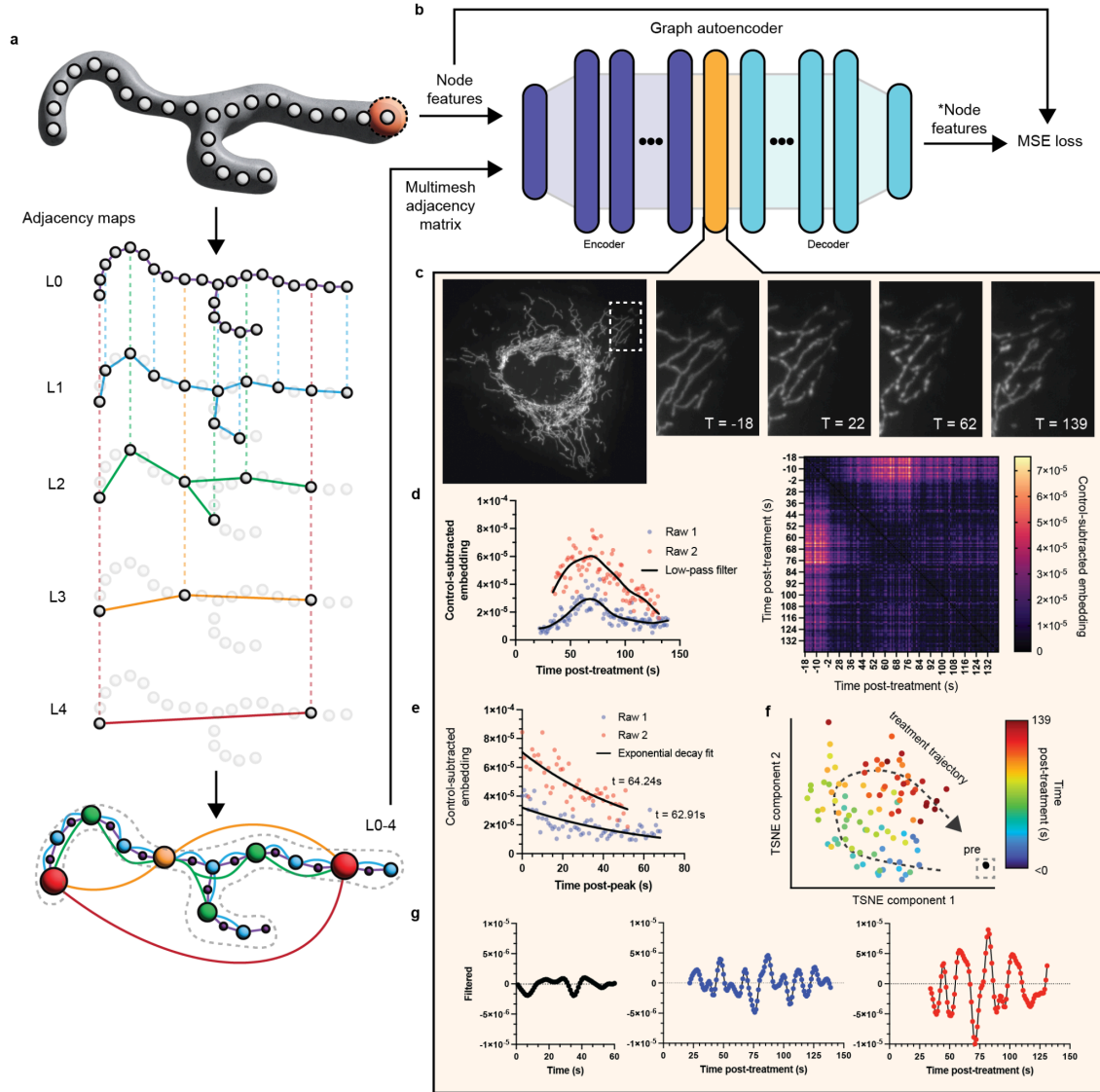


Fig. 5: Quantification of the evolution of Ionomycin-treated mitochondria multi-mesh graphs via comparisons of graph autoencoder latent space embeddings.

a. Example construction of a multi-mesh adjacency network of a mitochondrion, where each level (L) corresponds to the power-of-2 node-jump distance used for node linkage at that level, allowing for efficient message-passing at variable ranges within one organelle. **b.** The multi-mesh adjacency matrix (node edges) and node features are used as the inputs to a graph autoencoder. The GNN uses an MSE loss derived from the comparisons on the differences of the input and output node features for unsupervised training. After training, the latent space representation outputs (orange) from the encoder can be used for vector-based similarity comparisons. **c.** Fluorescently labeled mitochondria with representative images throughout their responses to Ionomycin treatment. **d.** Cosine distances of latent space embeddings to the average of the 18 pre-treatment latent space embeddings for two independent samples (left), or to all latent space embeddings (right) of mitochondria multi-mesh graphs after Ionomycin treatment. Raw 1 corresponds to the representative images in c. **e.** Cosine distances of latent space embeddings to the average of the 18 pre-treatment latent space embeddings post-peak, fit to exponential decay curves. **f.** t-SNE dimensionality reduction of latent space embeddings colored by time post-treatment. **g.** Band-pass filtered cosine distances of latent space embeddings of untreated mitochondria to the first frame's mitochondrial latent space embeddings (left) or of Ionomycin treated mitochondria to the first pre-treatment frame's mitochondrial latent space embeddings (middle and right).

the inputs from our original feature set dimension to 512 dimensions, followed by a sigmoid linear unit (SiLU), or Swish, activation function, and layer normalization⁴⁴. The encoder uses an independently weighted 16-layer graph neural network (GNN) with a linear MLP, again followed by Swish activation and layer normalization, with a mean aggregation message passing step across the multi-mesh and a final residual connection for each layer^{45,46}. The decoder is similarly composed of 16 independently weighted layers, but instead uses a graph attention network (GAT) operator with a 20% dropout, followed again by a Swish activation function, layer normalization, and a residual connection⁴⁷. Finally, we transform the 512 features back to the original feature set's dimensions.

Our case study focuses on examining mitochondrial networks in cells treated with Ionomycin, a calcium channel depolarizer known to induce fission-like events in mitochondria⁴⁸. Before treatment, we capture 20 volumes of fluorescently tagged mitochondria at a frequency of 1Hz (1 volume per second), leading to 18 pre-treatment graph embeddings (Fig. 5c). We then treat the cells with 4 uM of Ionomycin, and begin imaging for up to 120 volumes, again at 1Hz. We run the dataset through feature extraction with Nellie, construct its multi-mesh graph, and normalize the nodes' features to zero mean and unit standard deviation. To train the model, we use a 70/30 train/test split of our data and use an MSE loss to compare the reconstructed features to the original normalized features during training. We run the training with an Adam optimizer and a learning rate of 0.01 until validation loss stops decreasing for more than 10

epochs⁴⁹. We use the model with the lowest validation loss as our final model, which was achieved after only 40 epochs (Extended Data Fig. 11).

Post-training, we deployed the model's encoder to obtain latent space representations of each node across different timepoints. These embeddings allowed us to geometrically compare graphs between temporal frames via cosine distances, revealing distinct phases in the mitochondrial network's response to Ionomycin treatment. A control graph embedding was established by averaging the 18 temporal frames' pre-treatment graph embeddings, serving as a baseline for comparison. The cosine distance to the control embedding delineated a consistent period of alteration and gradual recovery post-treatment (Fig. 5d). We see that, compared to the control graph, Ionomycin shows a quick rise (~60s to the peak) followed by a recovery nicely modeled by an exponential decay (tau of ~63s) (Fig. 5e). Using t-SNE for dimensionality reduction, we visualize the divergence and eventual convergence of post-treatment graph embeddings towards the pre-treatment group, whose 18 points are essentially in the same position on the t-SNE plot (Fig. 5f)⁵⁰. Surprisingly, we identify oscillatory patterns in the graph embeddings post-treatment, absent in pre-treatment embeddings (Fig. 5g). These oscillations, discerned via frequency-based bandpass filtering and Fourier analysis, suggest intriguing mitochondrial responses to Ionomycin treatment that are ripe for exploration, but whose analyses and interpretations lie outside the scope of this paper.

This study demonstrates a novel method for analyzing organellar organization and motility using graph-based latent space representations. The approach offers rich, exploratory insights into cellular dynamics, akin to cell-painting strategies in drug discovery. The potential applications of this technique are vast, ranging from rare event detection in single organelles, to detailed organelle network studies, to broader systemic analyses in various model systems, and can be expanded to graph-representations of other structures at both larger and smaller resolutions. We hope that this case study will inspire further innovative research in organellar microscopy, leveraging the power of graph-based analyses to uncover new dimensions in cellular biology.

Discussion

Nellie is an unbiased and efficient pipeline for accurately and automatically analyzing spatial and temporal features of organelles, while staying agnostic to the organelle or substructure in question. We use intracellularly optimized adaptive preprocessing to allow for multi-scale segmentation, and adaptive local peak detection to generate multi-scale markers for tracking. Our motion capture marker linkage method uses the most important regions in our data as waypoints, independent of instance segmentations, while our flow interpolation method allows for tracking of sub-voxel coordinates. Finally, our multi-level feature extraction allows cross-sectional and hierarchical analyses both within and between scales of interest. This allows users to interpret their data from a sub-voxel level, all the way up to an image-wide level. Conveniently, we package our methods in a Napari plugin to allow for visualization and point-and-click functionality for ease-of-use, while keeping the codebase modular to allow flexibility and extensibility for more advanced users⁵¹.

The case studies we presented show Nellie's broad range of applications were two-fold. First, we demonstrated Nellie's ability to capture extensive metrics in both Golgi and mitochondria by using object and branch-based morphology and motility features to train random forest models and predict organelle type. These useful results set the stage for performing multi-organellar fluorescence imaging in single channels, extending the information available from microscopy datasets. Second, we were able to construct multi-level mesh-like graph networks of mitochondria, which we used to train an unsupervised graph autoencoder, allowing for efficient variable-range message passing

between nodes. From this trained autoencoder, we were able to compare latent space embeddings of the graph nodes to investigate the effect of ionomycin on mitochondrial networks, such as intrinsic feature oscillations and post-treatment effect-and-recovery dynamics. To our knowledge, this case study also establishes the first organelle-based graph autoencoder, a model that would not be possible without high quality segmentation and tracking, and a diverse and comparable feature set, both of which were only possible through Nellie. We predict this organelle graph autoencoder type of model to have a broad and useful range of applications, from treatment-based clustering and comparisons of organelles, reminiscent of Cell Painting methods, to local morphology and motility predictions of organelles, reminiscent of GraphCast's weather prediction, but at intracellular scales^{31,52}.

We hope Nellie will promote imaging-based approaches for analyzing organelles and their perturbation-mediated disruptions. Additionally, we hope Nellie's ease-of-use will encourage open-access science by providing a simple way to share intracellular feature data in a comparable manner. We present Nellie as a catalyst for a new wave of scientific inquiry, where the complex weave and elaborate dance of organelles is not just observed, but deeply understood, and where the mysteries of the cell are unlocked, one pixel at a time.

Methods

Cell culture

U2OS osteosarcoma cells used in the representative figures throughout the main text, and in the multi-mesh GNN case study were cultured following standard procedure at 37°C with 5% CO₂ in DMEM (Thermo #10567014) supplemented with 10% fetal bovine serum (Gibco #26140-079). Cell passaging occurred every 3-5 days, and downstream assays were performed before reaching 20 passages of growth. For the organelle unmixing case study, U2OS cells were cultured in DMEM supplemented with 10% FBS, 1X antibiotic-antimycotic solution and 1X GlutaMAX (Gibco).

Fluorescent labels

To establish a stable cell line expressing a fluorescently labeled version of COX8A, a mitochondrial matrix protein, for representative images throughout the main text and the multi-mesh GNN case study, U2OS cells at passage #8 (one million cells) were transfected with 1ug of DNA (Davidson-COX8A-mEmerald construct, Addgene code 54160) using the SE Cell Line Nucleofector Kit (Lonza #V4XC-1032) following the manufacturer's protocols. Transfected cells were cultured on collagen-coated plates to facilitate the recovery process. After two days, cells were selected with 1mg/ml Geneticin Selective Antibiotic (G418 Sulfate, ThermoFisher #10131035) for a week. Fluorescence signals were continuously monitored during the selection process. Upon recovery, G418 at a concentration of 0.5 mg/ml was used for stable cell line maintenance. FACS-sorting for moderate-expression cells was performed to enhance the homogeneity of cells containing labeled mitochondria. Lysosome staining was

performed via a 30 min incubation of 1 μ M SiR-Lysosome (Cytoskeleton #CY-SC012) and washed out 2x with warm media.

To generate U2OS cells expressing three genetically encoded fluorescent markers targeted to organelles for the organelle unmixing case study, a plasmid was generated containing mEGFP targeted to the mitochondrial matrix with a human COX8 presequence, ECFP-tagged H2B, and the first 82 residues of B4GALT1 tagged with mScarlet. MluI and AsiSI sites were used to insert left and right homology arms, respectively, for the CLYBL safe harbor locus flanking the coding sequence. 2 homozygous knock-in clones were generated in U2OS cells (ATCC #HTB96) using CRISPR editing. Clones were validated using Sanger sequencing of genomic DNA.

Image acquisition

Cells were plated on fibronectin coated (Sigma #F1141-1mg) 8-well glass-bottom chamber slides (CellVis #C8-1.5H-N) and incubated for 4 hours (main text figures and multi-mesh GNN case study) or 24 hours (organelle unmixing case study). Imaging was then performed on an in-house single objective light sheet microscope with a stage-top incubator maintaining a temperature of 37°C with 5% CO₂ throughout⁵³. Videos were acquired of individual cells at a frequency of 1 3D volume/second using 5% laser power and 1ms exposure, calculated to be 2.62 μ J per volume on the sample.

Treatments

Drug injections include the calcium ionophore, Ionomycin (4 μ M, Thermo #I24222).

Random forest classifier

For our random forest classifier, we use the same hyperparameters across all three models - motility only, morphology only, and motility and morphology combined - to discriminate against mitochondria and Golgi within our organelle demixing case study.

The random forest classifier is implemented via scikit-learn's RandomForestClassifier class, with the following hyperparameters: `n_estimators=300`, `criterion='gini'`, `max_depth=None`, `min_samples_split=2`, `min_samples_leaf=1`, `min_weight_fraction_leaf=0.0`, `max_features='sqrt'`, `max_leaf_nodes=None`, `min_impurity_decrease=0.0`, `bootstrap=True`, `oob_score=False`, `n_jobs=-1`, `random_state=42`, `verbose=0`, `warm_start=False`, `class_weight=None`, `ccp_alpha=0.0`, `max_samples=None`, `monotonic_cst=None`.

For the motility only model, the median, maximum, minimum, and standard deviation values of the following features are used as inputs: the angular velocity magnitude w.r.t. the branch's pivot point between t1 and t2 (`rel_ang_vel_mag_12`), the angular acceleration magnitude w.r.t. the branch's pivot point (`rel_ang_acc_mag`), the linear velocity magnitude w.r.t. the branch's pivot point between t1 and t2 (`rel_lin_vel_mag_12`), the linear acceleration magnitude w.r.t. the branch's pivot point (`rel_lin_acc_mag`), the linear velocity magnitude of the branch's pivot point between t1 and t2 (`ref_lin_vel_mag_12`), the linear acceleration magnitude of the branch's pivot point (`ref_lin_acc_mag`), the directionality of the branch w.r.t. the center of mass of the fluorescence intensity between t1 and t2 (`com_directionality_12`), and the rate of

change of the directionality w.r.t. the center of mass of the fluorescence intensity (com_directionality_acceleration).

For the morphology only model, the following features are used as inputs: area, extent, solidity, the minimum, median, and maximum of the object's inertia tensor eigenvalues (inertia_tensor_eig_sorted_min, inertia_tensor_eig_sorted_mid, inertia_tensor_eig_sorted_max), the total length (branch_lengths), the average radius (branch_radius), the average tortuosity (branch_tortuosity), and the average aspect ratio (branch_aspect_ratio).

For the morphology and motility combined model, all the features from both the morphology and motility models were aggregated.

For both training and testing, all feature columns were first standardized (mean of 0, standard deviation of 1), then used as inputs to the random forest classifier.

**Nellie: Automated organelle segmentation, tracking,
and hierarchical feature extraction in 2D/3D live-cell microscopy**

Supplementary Materials

Austin E. Y. T. Lefebvre^{1,*}, Gabriel Sturm^{1,2}, Ting-Yu Lin¹, Emily Stoops¹, Magdalena Preciado López¹, Benjamin Kaufmann-Malaga¹, Kayley Hake¹

¹Calico Life Sciences LLC, South San Francisco, CA, 94080

²Department of Biochemistry and Biophysics, University of California San Francisco,
San Francisco, CA, 94158

*Address correspondence to

Austin E. Y. T. Lefebvre, Ph.D.
Calico Life Sciences
1170 Veterans Blvd
South San Francisco, CA, 94080
Email: austin.e.lefebvre+nellie@gmail.com

Supplementary Note 1: Optimization of multi-scale Gaussian filtering for anisotropic images in cellular fluorescence microscopy datasets

In our study, the establishment of minimum and maximum radii for filtering operations is guided by the specific parameters of the imaging metadata, ensuring an alignment with the physical dimensions represented within the dataset. The lower bound for the radius is determined by selecting the greater of two values: a predefined threshold of 0.20 micrometers, which approximates the diffraction limit of light, or the pixel size in the X dimension of the image. This approach ensures that the filtering scale remains relevant to the resolution characteristics of the dataset. Conversely, the upper bound is uniformly set at 1 micrometer, marking the maximal scale of interest for our analysis. These radii are subsequently translated into pixel/voxel dimensions.

For the Gaussian filtering process, we derive the minimum and maximum sigma values directly from these pixel-based radii, applying reduction factors of one-half and one-third, respectively. This strategy is designed to calibrate the filter's sensitivity to features of varying intracellular sizes. To span the range of feature scales, we implement a series of five sigma values, ensuring comprehensive coverage across the standard deviation spectrum. The inter-sigma step size is calculated to bridge the desired feature scales effectively, imposing a minimum threshold on step size to prevent redundantly small increments that yield negligible changes in filtering outcomes. This structured approach yields a discrete set of sigma values, each corresponding to a specific standard deviation within the Gaussian filtering framework, thus enabling the filter to adaptively respond to biological features of different scales.

In addressing the challenge of anisotropic datasets prevalent in microscopy imaging – characterized by equivalent resolutions in the X and Y axes but reduced resolution along the Z axis – it is imperative to adjust the kernel values of 3D convolutional filters. This adjustment is critical within our preprocessing framework, which utilizes Gaussian filters across a multi-scale parameter space in both Frangi and Laplacian of Gaussian filtering applications. To counteract anisotropy, we construct a sigma vector for each scale, maintaining uniform standard deviations for the X and Y dimensions while adapting the Z dimension's standard deviation in accordance with the voxel resolution ratio (Z/X). This methodology ensures a consistent filtering effect across the dataset, irrespective of inherent resolution variances. In 2D datasets, which are exempt from anisotropic concerns, a singular sigma value is employed without modifications for anisotropy.

Supplementary Note 2: The Minotri threshold

In this study, we introduce the Minotri threshold approach - a fusion of the Otsu and Triangle methods, adapted to the unique challenges of automated organelle segmentation.

The Otsu method is well known for its capability to segment images based on a bimodal intensity distribution. It accomplishes this by calculating a threshold that maximizes the between-class variance, effectively distinguishing between the foreground (organelles) and the background. Otsu's algorithm excels in scenarios where the histogram exhibits two distinct peaks, corresponding to these two classes. In such cases, it tends to favor the class with the larger peak, thus ensuring the majority of the pixels from this peak are classified correctly. However, its performance may be less optimal in images with skewed histograms or those lacking a clear bimodal distribution.

On the other hand, the Triangle method approaches thresholding from a geometric perspective. It identifies the threshold by drawing a line from the peak of the histogram to the farthest end and then finding the point on the histogram that is furthest from this line. This method is particularly effective in dealing with histograms that are not bimodal or are skewed, such as in cases where there is a smooth transition from foreground intensity to background intensity, or when there is a large amount of diffuse background signal, whose intensity lies within a distribution higher than the background but lower than the foreground, making it a versatile tool for images where Otsu's method might struggle.

Our Minotri threshold approach combines these two methodologies by adopting the minimum (min) of the thresholds determined by the Otsu (ot) and Triangle (tri) methods. This approach ensures a more nuanced and adaptable segmentation, particularly useful in microscopy images where intensity distributions can vary significantly. By choosing the lower threshold, we err on the side of inclusivity, capturing a broader range of (both photon density-based and structurally based) intensities that represent the organelles, while still maintaining a rigorous standard for segmentation quality. This strategy is especially beneficial in cases where one method may yield a threshold that is too high, potentially excluding relevant structural information.

By integrating the Minotri threshold into our segmentation workflow, we achieve a balance between sensitivity and precision. This approach allows for the robust detection of structures across a wide range of intensity distributions, thereby enhancing the accuracy and reliability of our semantic segmentation process. This combined thresholding technique offers a versatile and effective tool for the detailed study of diverse organelles.

Supplementary Note 3: Frangi filter parameter selection

Though the Frangi filter, which uses the eigenvalues of the Hessian matrix of the image as attributes, is historically used to accentuate vessel structures within images, it also works exceptionally well at accentuating structural components in general, as long proper Frangi parameters and scale ranges over which to run the filter are chosen. As organelle shapes vary dramatically both between and within different types of organelles, we must carefully balance the Frangi filter's parameters and scale range in order to properly capture this diversity without accentuating any specific type of organelle.

The alpha parameter controls the sensitivity of the filter to the deviation from a blob-like structure. In the context of structure detection, it helps in distinguishing between disc-like, blob-like, and tube-like structures based on the eigenvalues of the Hessian. In practice, a lower alpha value makes the filter more sensitive to disc-like structures and less sensitive to tube-like structures, while increasing alpha will do the opposite, making the filter less responsive to blob-like and disc-like structures and more focused on tube-like features. We set alpha-squared to 0.5, giving the filter a moderate sensitivity to blob-like structures (Extended Data Fig. 2). This allows the filter to be balanced in its response to tube-like structures and blob-like structures. This setting means the filter will enhance tubular structures while still allowing for some degree of response to blob-like features. It won't be overly discriminative against structures that slightly deviate from the traditionally Frangi-directed tubular shape.

The beta parameter controls the filter's sensitivity to the deviation from a disc-like structure. It is directly involved in the suppression of the response of the filter to disc-like and blob-like structures. In practice, adjusting beta alters the filter's response to different types of structures. A lower beta value increases the sensitivity of the filter to disc-like structures, while a higher beta value makes the filter more selective for tubular structures. We also set beta-squared to 0.5, giving a moderate level of suppression for disc-like structures (Extended Data Fig. 2). This prevents the filter from being overly aggressive in suppressing disc-like features.

The gamma parameter is a scaling parameter that controls the sensitivity of the filter to the overall magnitude of the eigenvalues. This parameter essentially acts as a normalization factor in the function. In practice, changing gamma affects the filter's sensitivity to the background noise and contrast of the image. A higher gamma value can suppress the response of the filter to areas with low contrast, reducing the likelihood of detecting false positives due to noise. Conversely, a lower gamma would increase sensitivity to lower contrast regions but would also increase vulnerability to noise. This is the most important parameter to set properly, as poor gamma selection will lead to failure in correctly thresholding regions of interest post-filtration. By automating the gamma selection process by deriving it from the Minotri threshold, we're linking gamma to the inherent contrast characteristics of the image at that scale. This is a novel way to make the filter's response adaptive to each specific scale's contrast profile. This is particularly useful where samples can vary greatly in their staining, illumination, and intrinsic structural contrast. Additionally, by adapting gamma using our

Minotri threshold method at each scale independently, we automatically adjust gamma to enhance subtler structures in low-contrast images, while in high-contrast images, it prevents over-enhancement and preserves detail. This ensures that the filter's sensitivity to the eigenvalue magnitudes is tailored not just to the image's overall contrast profile, but also to the contrast profile relevant to structures at each specific scale. This means for finer scales (smaller Gaussian sigma) which targets smaller structures, the gamma value will adapt to the contrast nuances at that scale, and similarly for larger scales.

Supplementary Note 4: Preprocessing refinement techniques for structural contrast enhancement

Following the initial multi-scale structural enhancement of organelles, the pipeline incorporates further post-preprocessing techniques to refine the output images. The refined post-preprocessing begins with the application of a masking technique to the preprocessed image, aiming to eliminate regions with minimal structural information. This is achieved by setting a threshold that masks regions falling below the 1st percentile of non-zero pixel values. This ensures a focus on regions rich in meaningful content. Subsequently, a binary opening operation is performed on the mask to smooth out noise within the structures. This morphological operation, involving erosion followed by dilation, refines the mask's boundaries, and removes spurious pixels that could detract from the integrity of the analysis. These post-preprocessing steps collectively ensure that the pipeline produces refined output images. This approach not only enhances the visibility of organelles but also prepares the images for accurate segmentations of regions of genuine structural significance.

2D datasets typically have reduced structural noise compared to 3D datasets, which can be attributed to several potential factors, including the reduced complexity of organelles that can be captured in a single plane, compared to the three-dimensional complexity of organelles in ZYX datasets. Furthermore, anisotropy present in 3D datasets - where differences in resolution between the XY plane and the Z-axis lead to variability in structural clarity - typically necessitates more complex filtering approaches to achieve uniform enhancement across all dimensions. The Frangi filter, optimized for

enhancing vessel-like structures, also exhibits differential effects in 2D versus 3D datasets due to these dimensional and anisotropic considerations. Due to the increased structural noise in 3D datasets (ZYX), an additional refinement step involves the application of a multi-scale Laplacian of Gaussian (LoG) filter. This filter accentuates structural details and smooths out noise, which is particularly prevalent in three-dimensional imaging due to anisotropy. The choice of a multi-scale approach allows for effective enhancement across different structural scales, ensuring both broad and fine details are captured with precision.

Supplementary Note 5: Considerations on the application of the hole-filling algorithm in 2D and 3D segmentation

The segmentation process for organelles incorporates a binary hole-filling algorithm exclusively in the analysis of 3D images. This decision is informed by distinct considerations regarding the structural characteristics and noise levels inherent to 2D versus 3D datasets.

One of the primary reasons for omitting the hole-filling algorithm in 2D segmentation is the inherently lower level of structural noise within these datasets. The simplified nature of 2D imaging, capturing a single plane of focus, generally results in clearer delineation of organelles. This clarity reduces the likelihood of generating the types of internal inconsistencies within segmented organelles that the hole-filling algorithm is designed to address.

The decision to apply the hole-filling algorithm selectively also stems from the geometric considerations of organelles across dimensions. In 2D images, closed circular organelles are common, and applying hole-filling indiscriminately would lead to the undesired effect of filling these circles, potentially obscuring meaningful biological cavities. While the algorithm aids in creating a more consistent representation of such organelles by addressing internal voids, it operates under the assumption that spaces within the segmented organelles are artifacts rather than biologically relevant features. A notable caveat in the application of the hole-filling algorithm within 3D segmentation concerns the potential for erroneous interpretation of certain organelle geometries.

Specifically, if an organelle inherently forms a spherical shape with a central void (resembling a ball with an internal hole), the algorithm may inappropriately fill this void. This limitation underscores a challenge in distinguishing between genuine biological internalized cavities and segmentation artifacts, particularly in the context of 3D structural complexity. If spherical shapes with central voids are important for the user's analysis, we suggest replacing this binary hole filling with a binary closing operation below the scale of the object of interest.

Supplementary Note 6: Efficient distance transformation using k-dimensional trees

In this section, we introduce, to our knowledge, the first application of a k-dimensional (k-d) tree for a computationally efficient distance transformation of a binary mask. The process begins with the generation of a border mask, which delineates the periphery of the organelles within the binary mask. This is accomplished by subtracting the original binary mask from its one-voxel binary dilation. Binary dilation incrementally expands the boundaries of the organelle. The subtraction operation thus isolates a thin border that precisely maps the outermost edge of each organelle, effectively creating a mask that represents the interface between the organelle and its surrounding environment.

Following the creation of the border mask, the next step involves constructing a k-d tree from the coordinates of the border pixels. The k-d tree is a space-partitioning data structure optimized for organizing points in a k-d space, facilitating efficient queries for nearest neighbors. In the context of our method, the k-d tree serves as a computational framework that allows for rapid identification of the closest border pixel for any given voxel within the instance segmentation mask of organelles.

With the k-d tree in place, the final step is to perform a distance transformation on the binary mask. This is achieved by querying the k-d tree with the coordinates of all voxels in the instance mask. For each voxel, the k-d tree identifies the nearest border pixel and calculates the Euclidean distance between these two points. This process is repeated for every voxel in the mask, resulting in a distance-transformed image where the value

of each voxel reflects its minimum distance to the organelle's boundary. By employing a k-d tree for the nearest-neighbor search, our approach minimizes computational overhead, enabling rapid processing of large datasets without sacrificing accuracy.

Supplementary Note 7: Methodology for multi-scale and adaptive local maxima detection

Initially, the distance-transformed image undergoes filtering using a Laplacian of Gaussian (LoG) filter, incorporating a set of sigma values identical to those utilized in the preprocessing pipeline. The LoG filter, by design, enhances regions of rapid intensity change, which are indicative of edges and, by extension, potential peak points within the organelles. The application of this filter across multiple scales allows for the detection of peaks that correspond to features of varying sizes, ensuring comprehensive coverage of the intracellular structural landscape (Extended Data Fig. 6).

Following LoG filtering, a maximum filter is applied to the resultant multi-scale filtered images. This process involves comparing each voxel to its neighbors within a defined footprint, retaining only those voxels that represent the highest value. By conducting this operation across the stacked LoG filtered images, voxels that retain their maximal value in the corresponding volume slice of the LoG filtered image are classified as local maxima for that specific scale. The identified local maxima across all scales are then compiled into a single stack of images. This stack is subsequently flattened, consolidating the peak points into a singular image that serves as the basis for motion capture marker identification. This flattened image, rich in peak coordinates, effectively highlights the most prominent features within the organelles, earmarking them for feature extraction and downstream temporal linkage.

Given the potential for closely situated peaks to complicate (due to redundancy) rather than enhance subsequent analyses, an additional refinement step is employed. This step involves assessing the intensity of each peak within the original image and applying a proximity-based selection criterion. Peaks deemed too close to one another are subjected to a comparison of their respective intensities, with preference given to the peak of higher intensity. This is facilitated by the construction of a k-d tree from the sorted peak coordinates, enabling efficient nearest-neighbor searches to identify and eliminate proximal peaks that fall within a predefined minimum distance threshold.

Supplementary Note 8: Temporal continuity in organelle tracking via forward and backward interpolation of semantic segmentations across frames

Nellie includes an optional, but highly requested component for tracking instance segmentations of individual organelle objects between adjacent frames. This feature allows for the extraction of motility features and changes in morphology of a specific label across multiple temporal frames. Specifically, we maintain continuity in the identification of labeled organelle voxels across frames by sequentially relabelling adjacent frames via both a forward and backward interpolation scheme from a temporal frame T of interest (Extended Data Fig. 7).

For forward relabelling from frame t to $t+1$, forward interpolation of motion vectors for all semantic segmentation mask voxels in frame t is performed, yielding interpolated coordinates at frame $t+1$. Similarly, backward interpolation of motion vectors for all semantic segmentation mask voxels in frame $t+1$ is carried out, providing interpolated coordinates at frame t . Next, frame t voxels are matched to the closest frame t interpolated coordinates derived from frame $t+1$ voxels, and vice versa. Matches are only considered if they are within the maximum travel distance threshold (1 $\mu\text{m/s}$). Unique matches are then assigned using a heap in-place priority queue based on the distance between the voxel and interpolated coordinate match. This prioritization ensures that the most accurate matches are assigned first, enhancing both computational efficiency and matching accuracy. Any unlabelled voxel in frame $t+1$ is assigned the label of its nearest relabelled voxel, provided the distance is within the

maximum travel distance threshold. This relabelling process is repeated until all voxels are labeled or until the number of unlabelled voxels stabilizes between iterations.

The backward relabelling process from frame t to $t-1$ mirrors the forward relabelling approach. First, forward and backward interpolations are conducted for frame $t-1$ and frame t voxels, respectively. Voxels from frame t are matched to the closest interpolated coordinates derived from frame $t-1$, and vice versa, within the maximum travel distance threshold. The assignment of unique matches and relabelling of unassigned voxels follows the same procedure as in forward relabelling, ensuring consistency and accuracy across temporal frames.

Supplementary Note 9: Spatial and temporal feature extraction of hierarchical organelle levels, continued

Organelle features are extracted hierarchically, with voxels representing the smallest unit of measured space, followed by nodes, which are skeleton voxels plus their surrounding radius-dependent voxels, followed by branch components, which are semantic segmentations of skeleton branches and their surrounding voxels, followed by organelles, which are semantic segmentations of connected components, followed finally by the organellar landscape, representing the entire image. Each larger component in the hierarchy also gets aggregated statistics of features from the lower levels. We have described all of the extractable features and their respective variable names in Supplementary Table 1.

At the voxel level, local flow, structure, and fluorescence intensity information is captured. At frame T , a voxel's flow is interpolated from $T-1$ to T , and from T to $T+1$ to generate its independent linear and angular velocity and acceleration vectors, of which we can break down to its magnitude and normalized orientation vectors. We also choose, for each branch, a local pivot point, as well as the entire organellar landscape's center of mass, representing two different points of reference for two additional sets of linear and angular motility features. We can then extract a directionality component by calculating the voxel's motion with respect to these points of reference.

At the node level, we calculate neighborhood flow patterns, as well as the thickness of an organelle branch at that skeleton voxel. To extract flow patterns, we first retrieve all

the flow vectors associated with the voxels of that node. To calculate the convergence of flow vectors to that node's center, we calculate the mean direction of magnitude of all the node's voxels with respect to the node center from $T-1$ to T . A positive number indicates voxels are flowing towards that node from $T-1$ to T . In contrast, divergence is calculated in the same way as convergence, but from T to $T+1$. A positive number indicates voxels are flowing away from that node from T to $T+1$. Vergere is simply the sum of divergence and convergence, where a positive number would indicate a local bottleneck of flow, and a negative number would indicate some flow repulsion from that node. The magnitude variability of flow vectors at that node is simply the standard deviation of the node's voxels' flow vector magnitudes. The direction uniformity is the mean value of the dot product similarity matrix of the node's voxels' orientation vectors.

At the branch level, we calculate skeleton metrics such as length, thickness, aspect ratio, and tortuosity, as well as standard region properties such as area, axes lengths, and solidity and extent metrics. To calculate skeleton properties, we treat each network as a graph, composed of lone tip (no adjacent), tip (one adjacent), edge (two adjacent), and junction (>2 adjacent) voxels. We modify the skeleton graph by removing all junction voxels and replacing their neighboring edge voxels with tip voxels. Each tip-to-tip segment is considered one branch instance. To efficiently traverse this graph, we construct a distance matrix between all non-zero voxels in our skeleton and link voxels that are less than 2 voxels from one another, using only the lower diagonal to avoid duplicate matches. From these linkages, we can calculate the length of a branch as the sum distance of all linkages of that branches' voxels plus the voxel-to-border

distance of the tip nodes of that branch. If the branch consists of only a single lone node, we instead calculate the length of that branch to be 2 times the voxel-to-border distance of the node. From this length measurement we calculate the tortuosity of a branch, defined as its length divided by the tip-to-tip spatial distance. We calculate the thickness of a branch as its mean voxel-to-border distance times two, and its aspect ratio as its length divided by its thickness. For calculating the region's properties, we use Scikit-Image's regionprops function.

At the organelle level, we simply calculate the connected component's region properties, again via Scikit-Image's regionprops function.

Finally, at the organellar landscape (image) level, we simply allow all aggregate statistics of all other hierarchies to be stored for export.

Supplementary Note 10: Multi-mesh graph-based representation of cellular organelle networks

In the construction of the multi-mesh network from organelle segmentation masks, the methodology employs a systematic approach to transform the intricate spatial relationships of organelles into a structured graph representation. This transformation is achieved through a series of computational steps designed to map the skeletonized representations of organelles onto a graph where nodes represent skeleton voxels that carry features of their surrounding voxels, and edges that delineate the spatial connections between these nodes, capturing the underlying organizational topology of the organelle network.

The initial step involves the utilization of a k-d tree for the efficient identification of immediately neighboring nodes. This radius is chosen to ensure that all immediate neighbors in a cubic voxel grid are considered, facilitating the accurate representation of spatial adjacencies within the graph. Each node, corresponding to a skeleton voxel, is then associated with a list of its neighbors, excluding self-references, to establish the basic graph structure.

Subsequently, the algorithm identifies a starting node for the graph, preferentially selecting a node with a singular neighbor (a tip node) to anchor the construction process. In the absence of such nodes, indicating a closed network, the first node in the branch's list is selected by default.

The construction of the multi-level mesh within the graph is then initiated by calculating the jump distances from the start node to all other nodes within the network. This calculation employs a depth-first search algorithm, incrementally increasing the jump distance as the search progresses through the network. The jump distances serve as a basis for establishing a hierarchical structure within the graph, where connections between nodes are formed based on increasing powers of two. This hierarchical connectivity facilitates efficient message passing at multiple distances, enabling the graph to capture a wide range of spatial relationships within the organelle network.

For each scale within the multi-level mesh, the algorithm generates a list of nodes that are valid at that scale, determined by their jump distances. This selective inclusion of nodes at each scale allows for the dynamic adjustment of the graph's hierarchy, ensuring that both local details and global organizational patterns are adequately represented. The edges within the multi-scale edge list are then generated by direct accessibility queries within the graph, establishing connections between nodes based on their proximity and mutual accessibility across the different scales of the mesh.

This detailed and systematic approach to constructing the multi-mesh network from organelle segmentation masks and their respective skeletons encapsulates the complex spatial organization of organelles within a scalable and interpretable graph framework. By leveraging the principles of graph theory and computational geometry, the methodology provides a robust foundation for analyzing the dynamic alterations in

organelle organization, offering insights into the functional implications of spatial arrangements within cellular environments.

Supplementary Note 11: Graph autoencoder model construction for organelle multi-mesh network analysis

The graph autoencoder model is structured to transform multi-dimensional data into a comparable latent space and subsequently reconstruct the original data, aiming to retain significant biological features and spatial relationships. This allows for latent space analysis of encoded features and complex interactions within organellar networks. The graph autoencoder comprises an encoder for data compression and a decoder for data reconstruction, each built with layers specifically chosen for their effectiveness in graph-structured data processing.

The encoder initiates with a Multilayer Perceptron (MLP) to project the initial feature set into a 512-dimensional embedding. Following the MLP, a Swish (SiLU) activation function introduces non-linearity, enhancing the model's ability to capture complex patterns. Layer normalization is applied to ensure consistent training dynamics across layers by normalizing the layer outputs. The core of the encoder consists of 16 graph neural network (GNN) layers. These layers are designed for effective feature transformation and aggregation within the graph, utilizing mean aggregation for message passing. The independent weighting of each GNN layer allows for flexibility in learning distinct aspects of the data. Residual connections are incorporated to facilitate deeper learning without the vanishing gradient problem.

The decoder mirrors the encoder's depth but switches to graph attention network (GAT) layers. These layers leverage attention mechanisms to prioritize the most relevant

features from neighboring nodes, crucial for accurately reconstructing the original feature space from the compressed latent representation. Dropout is incorporated at a rate of 20% within the GAT layers to prevent overfitting by randomly omitting subsets of features during training. Similar to the encoder, the decoder employs Swish activation and layer normalization post each GAT layer, concluding with a transformation back to the original feature size. This design ensures that the decoder can effectively reconstruct the original data, highlighting changes in organelle configurations.

The initial embedding is essential for transitioning from the high-dimensional raw feature space to a more comparable representation without significant information loss. The MLP efficiently achieves this transformation, while the SiLU activation function is chosen for its property of smoothing nonlinearities, improving model performance over traditional ReLU functions. The choice of GNN layers for the encoder stems from their ability to capture the dependency and interaction between intra-organellar nodes in a graph. Mean aggregation is used for its simplicity and effectiveness in summarizing variable-range neighborhood information, essential for understanding the context of each organelle node within the network. The adoption of GAT layers for the decoder is motivated by the need for a nuanced reconstruction of the original data. The attention mechanism within GAT layers allows the model to focus on the most informative parts of the input graph, crucial for detailed and accurate data reconstruction. Layer normalization and residual connection components are integral to the model for maintaining stable learning rates across training and enabling the effective training of

deep networks by allowing information and gradients to flow through the network without diminishment.

The model implementation leverages PyTorch and PyTorch Geometric, facilitating efficient graph data processing and neural network operations^{54,55}. Training involves minimizing the Mean Squared Error (MSE) between the original and reconstructed datasets, with the Adam optimizer chosen for its adaptive learning rate capabilities, especially suited for sparse data commonly found in graphs.

Supplementary Table 1: Table of Nellie's output features

For each level of the organellar hierarchy, we extract a multitude of features, as described in Supplementary Note 9.

Voxels:

Feature description (units)	Output name
The structural intensity value of the voxel (A.U.)	structure_raw
The fluorescence intensity value of the voxel (A.U.)	intensity_raw
Linear velocity vector wrt local pivot point (um/s)	lin_vel_rel_raw
Linear velocity magnitude wrt center of mass (um/s)	lin_vel_mag_com_raw
Linear velocity orientation wrt local pivot point (N/A)	lin_vel_orient_rel_raw
Linear velocity orientation wrt center of mass (N/A)	lin_vel_orient_com_raw
Linear velocity orientation, no reference (N/A)	lin_vel_orient_raw
Linear velocity magnitude wrt local pivot point (um/s)	lin_vel_mag_rel_raw
Linear velocity magnitude, no reference point (um/s)	lin_vel_mag_raw
Linear velocity vector wrt local pivot point (um/s)	lin_vel_com_raw
Linear velocity vector, no reference point (um/s)	lin_vel_raw
Linear acceleration magnitude wrt local pivot point (um/s ²)	lin_acc_rel_mag_raw
Linear acceleration vector wrt local pivot point (um/s ²)	lin_acc_rel_raw
Linear acceleration magnitude, no reference point (um/s ²)	lin_acc_mag_raw
Linear acceleration magnitude wrt center of mass (um/s ²)	lin_acc_com_mag_raw
Linear acceleration vector wrt center of mass (um/s ²)	lin_acc_com_raw
Linear acceleration vector, no reference point (um/s ²)	lin_acc_raw
Movement directionality wrt local pivot point (N/A)	directionality_rel_raw
Movement directionality wrt center of mass (N/A)	directionality_com_raw
Movement directionality change wrt local pivot point (N/A)	directionality_acc_rel_raw
Movement directionality change wrt center of mass (N/A)	directionality_acc_com_raw
Angular velocity vector wrt local pivot point (rad/s)	ang_vel_rel_raw

Angular velocity orientation wrt local pivot point (N/A)	ang_vel_orient_rel_raw
Angular velocity orientation wrt center of mass (N/A)	ang_vel_orient_com_raw
Angular velocity orientation, no reference point (N/A)	ang_vel_orient_raw
Angular velocity magnitude, wrt local pivot point (rad/s)	ang_vel_mag_rel_raw
Angular velocity magnitude, wrt center of mass (rad/s)	ang_vel_mag_com_raw
Angular velocity magnitude, no reference point (rad/s)	ang_vel_mag_raw
Angular velocity vector, wrt center of mass (rad/s)	ang_vel_com_raw
Angular velocity vector, no reference point (rad/s)	ang_vel_raw
Angular acceleration magnitude wrt local pivot point (rad/s ²)	ang_acc_rel_mag_raw
Angular acceleration vector wrt local pivot point (rad/s ²)	ang_acc_rel_raw
Angular acceleration magnitude, no reference point (rad/s ²)	ang_acc_mag_raw
Angular acceleration magnitude wrt center of mass (rad/s ²)	ang_acc_com_mag_raw
Angular acceleration vector wrt center of mass (rad/s ²)	ang_acc_com_raw
Angular acceleration vector, no reference point (rad/s ²)	ang_acc_raw

Nodes:

Feature description (units)	Output name
Distance from the node center to the edge x2 (um)	thickness_raw
Uniformity of the angular velocity vector orientation of the voxels around that node (N/A)	ang_direction_uniformity_raw
Uniformity of the linear velocity vector orientation of the voxels around that node (N/A)	lin_direction_uniformity_raw
Variability of the angular velocity vector magnitude of the voxels around that node (rad/s)	ang_magnitude_variability_raw
Variability of the linear velocity vector magnitude of the voxels around that node (um/s)	lin_magnitude_variability_raw
The sum of the convergence and divergence of vectors to the node center (um/s)	vergere_raw
The convergence of the flow vectors of the voxels in the node to the node center (um/s)	convergence_raw

The divergence of the flow vectors of the voxels in the node from the node center (um/s)	divergence_raw
Summary statistics of the node's voxels' metrics (see above)	voxel aggregate metrics

Branches:

Feature description (units)	Output name
Label corresponding to its original temporal frame 0 label, assigned during voxel reassignment (N/A)	reassigned_label_raw
Number of pixels in the branch divided by number of pixels in the branch's convex hull image (N/A)	solidity_raw
Number of pixels in the branch divided by number of pixels in the branch's bounding box (N/A)	extent_raw
Minor axis length of an ellipse with the same normalized second central moments as the branch, scaled by the image resolution (um)	axis_length_min_raw
Major axis length of an ellipse with the same normalized second central moments as the branch, scaled by the image resolution (um)	axis_length_maj_raw
The number of pixels of the branch scaled by the image resolution (2D: um^2 3D: um^3)	area_raw
The branch's tips' euclidean distance divided by its length (N/A)	tortuosity_raw
The length of the branch divided by its median thickness (N/A)	aspect_ratio_raw
The length of the branch (um)	length_raw
Summary statistics of the branch's voxels' metrics (see above)	voxel aggregate metrics
Summary statistics of the branch's nodes' metrics (see above)	node aggregate metrics

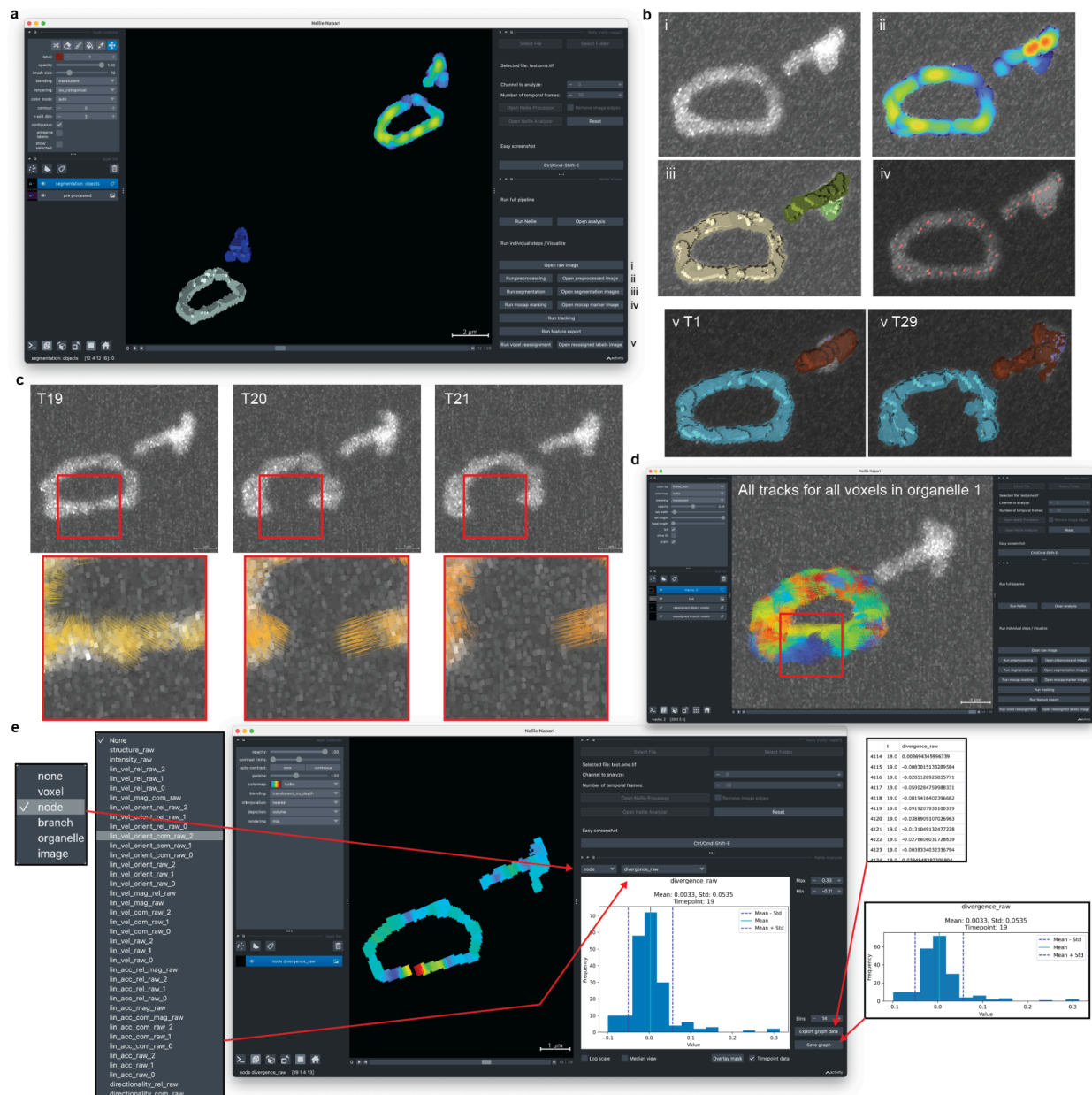
Organelles:

Feature description (units)	Output name
Label corresponding to its original temporal frame 0 label, assigned during voxel reassignment (N/A)	reassigned_label_raw
Number of pixels in the organelle divided by number of pixels in the organelle's convex hull image (N/A)	solidity_raw
Number of pixels in the organelle divided by number of pixels in the organelle's bounding box (N/A)	extent_raw

Minor axis length of an ellipse with the same normalized second central moments as the organelle, scaled by the image resolution (um)	axis_length_min_raw
Major axis length of an ellipse with the same normalized second central moments as the organelle, scaled by the image resolution (um)	axis_length_maj_raw
The number of pixels of the organelle scaled by the image resolution (2D: μm^2 3D: μm^3)	area_raw
Summary statistics of the organelle's voxels' metrics (see above)	voxel aggregate metrics
Summary statistics of the organelle's nodes' metrics (see above)	node aggregate metrics
Summary statistics of the organelle's branches' metrics (see above)	branch aggregate metrics

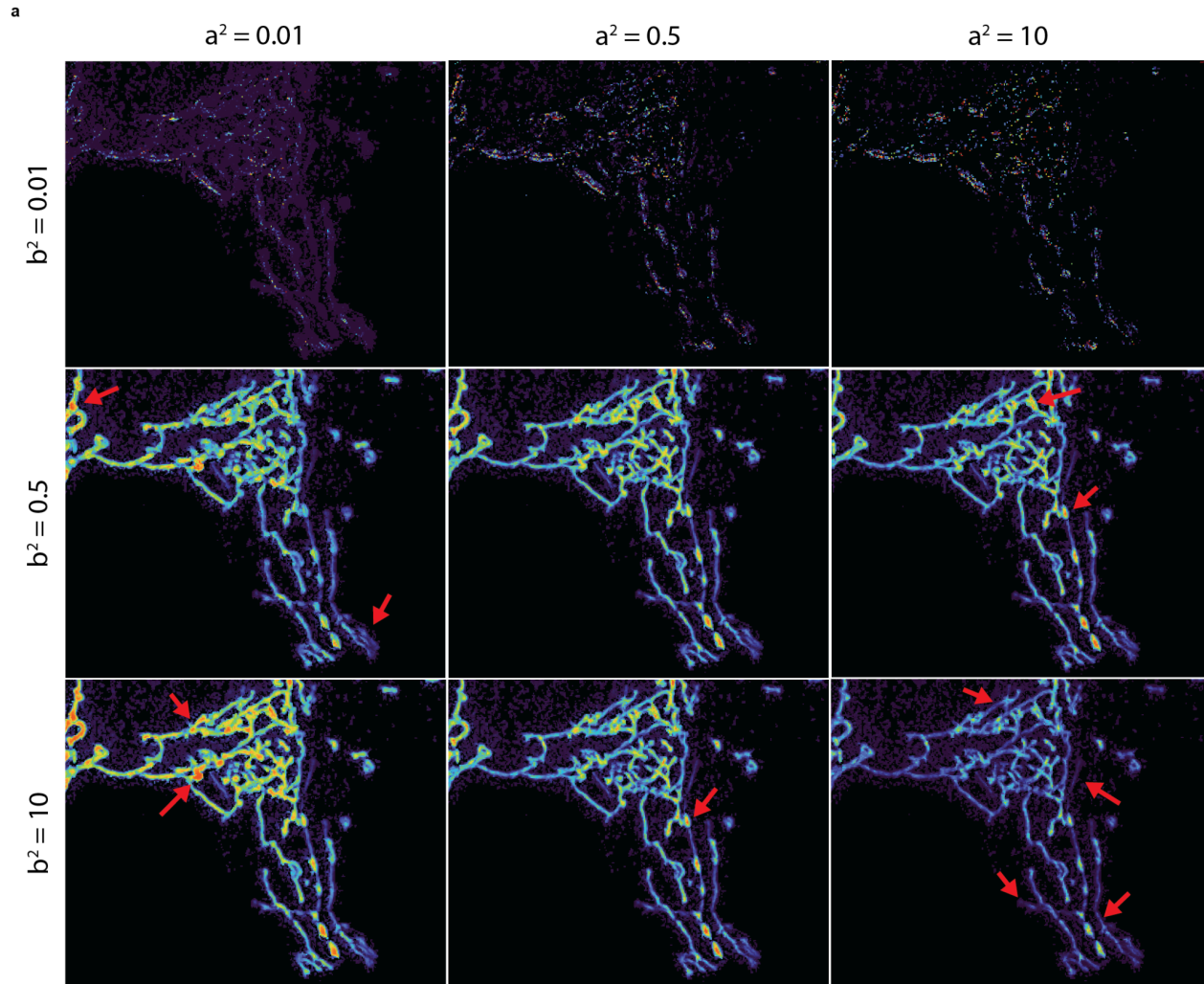
Image

Feature description (units)	Output name
Summary statistics of the image's voxels' metrics (see above)	voxel aggregate metrics
Summary statistics of the image's nodes' metrics (see above)	node aggregate metrics
Summary statistics of the image's branches' metrics (see above)	branch aggregate metrics
Summary statistics of the image's organelles' metrics (see above)	organelle aggregate metrics



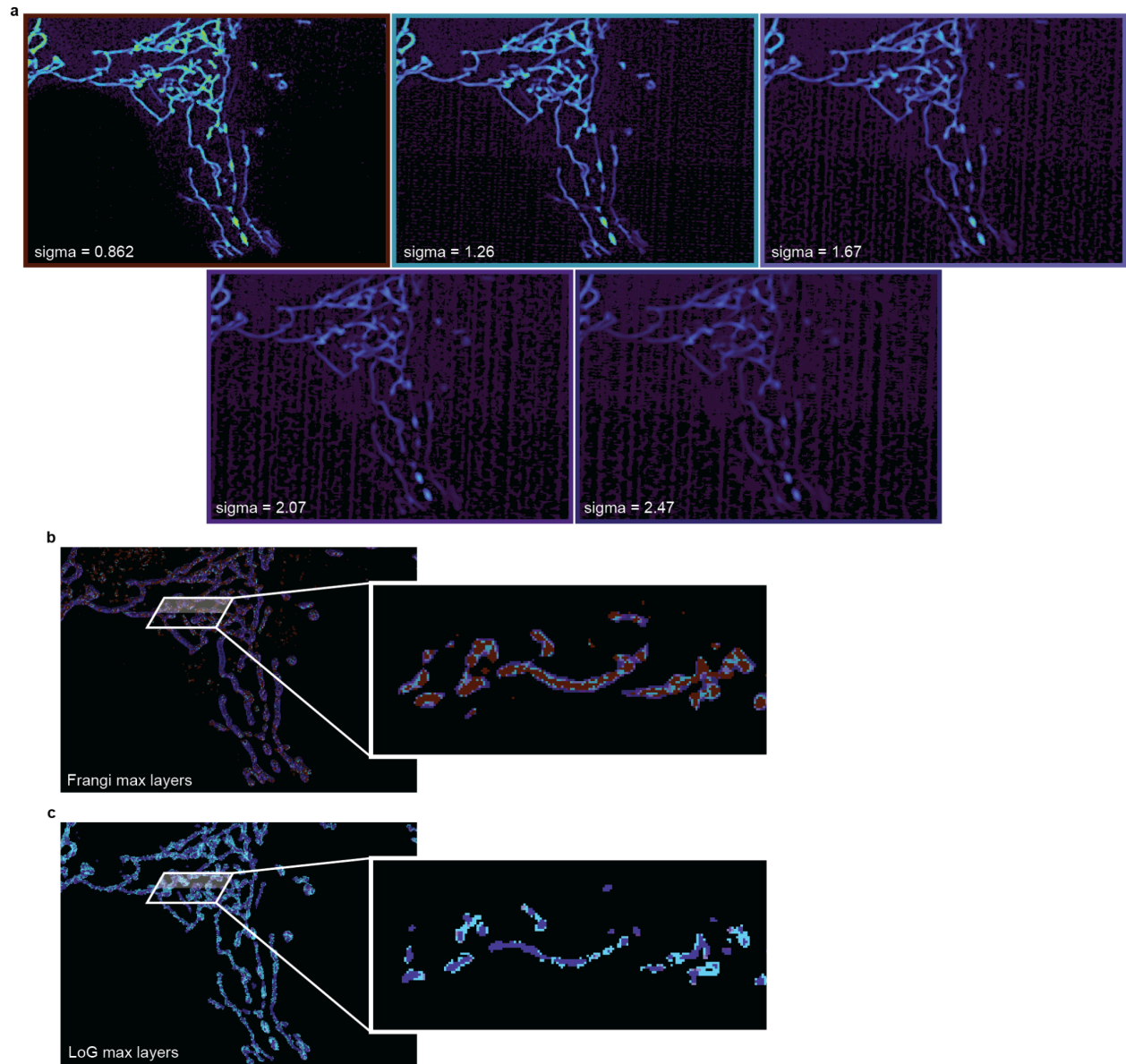
Extended Data Fig. 1: Nellie's Napari plugin makes organelle spatial and temporal hierarchical data processing and visualization easy to handle

a, Nellie's processing plugin is able to process individual files or batch process files. With individual files, Nellie can run individual steps at a time, and allow for visualization (**b**) of each part of the pipeline, including the raw image (**i**), the preprocessed image (**ii**), the instance segmentations of branches or organelles (**iii**), the mocap markers (**iv**), and the temporally-continuous relabelled branch and organelle instance segmentations (**v**). **c**, Nellie also allows for marking individual instance segmentations for track analysis, displaying tracks for all voxels of an object at that frame, as well as its interpolated tracks forwards and backwards across all time points (**d**). **e**, Nellie's analysis plugin allows for quick visualization and quantification of any of the available metrics, across any level of the hierarchy, with easy export buttons for every step.



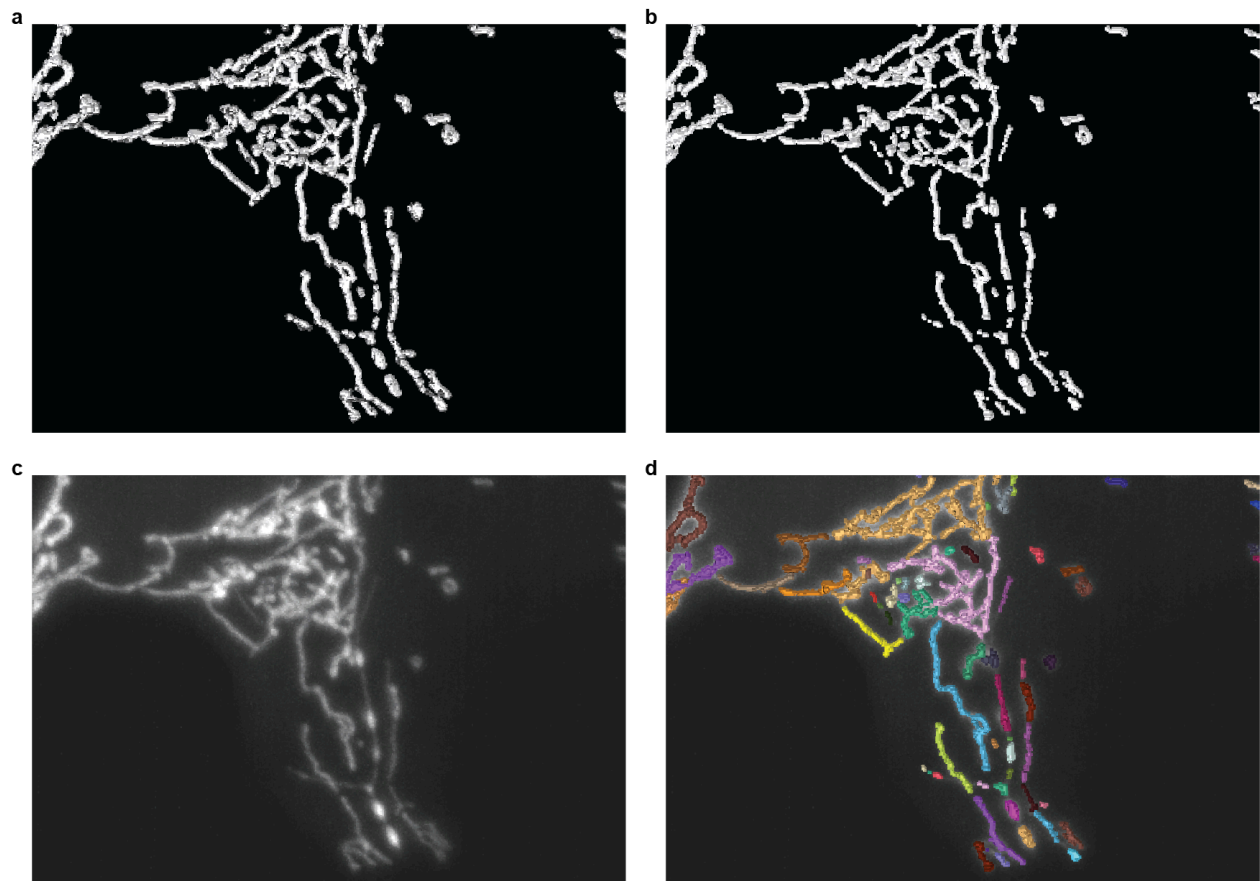
Extended Data Fig. 2: Frangi filter parameter effects on 3D structural contrast enhancement

a, A 3D fluorescently mitochondrial-labeled cell showcasing regions of tubular and blob-like structures. The outputs of the structural enhancement preprocessing using alpha and beta-squared Frangi filter parameters with alpha-squared ranging from 0.01 to 10 (columns), and beta-squared ranging from 0.01 to 10 (rows). The middle panel (0.5, 0.5) represents the hard-coded parameter set used in Nellie's pipeline. Red filled-in arrows show problematic regions.



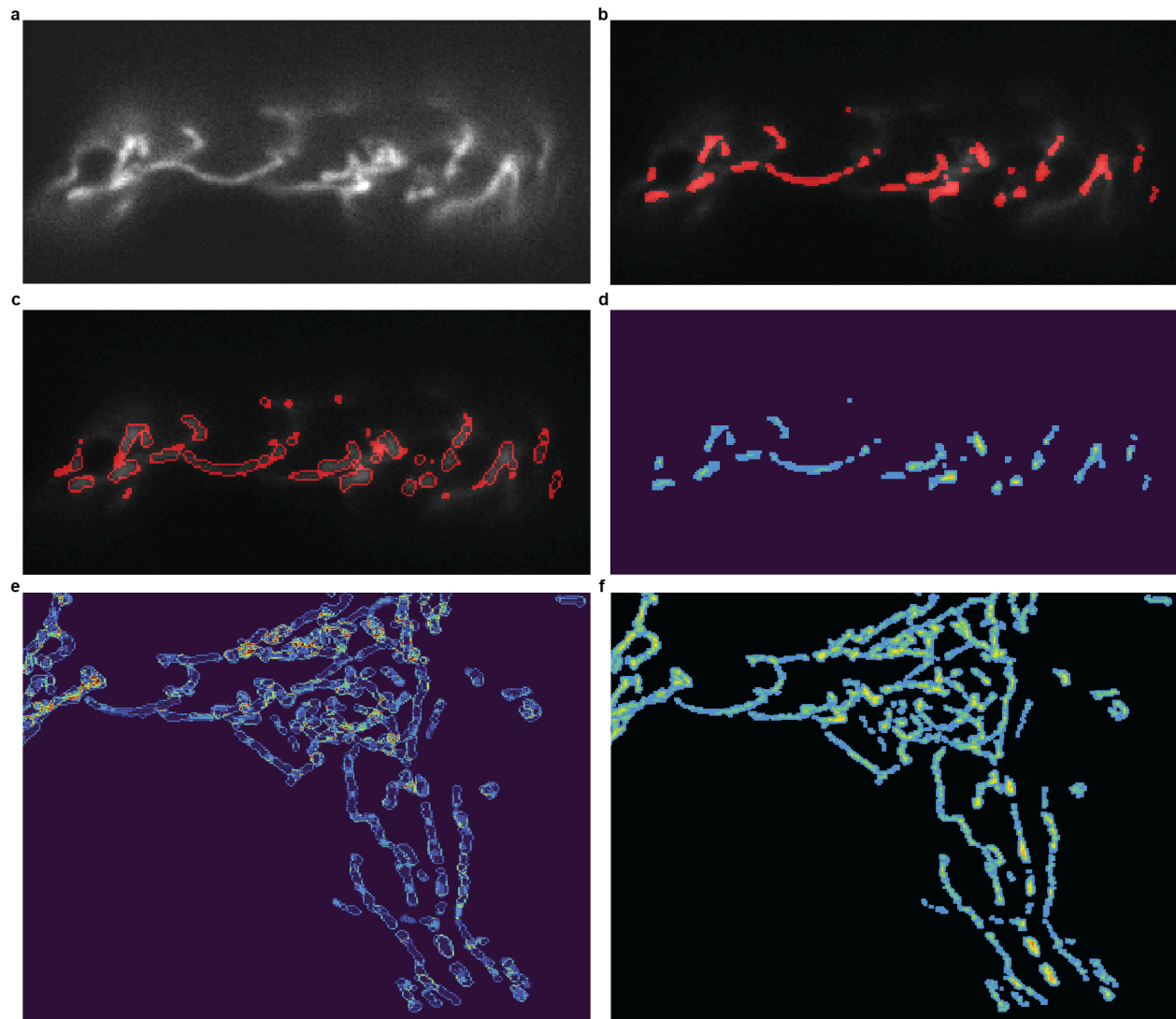
Extended Data Fig. 3: Contributions of preprocessing multi-scale intermediates

a, A 3D fluorescently mitochondrial-labeled cell run through a Frangi filter at 5 different scales, undergoing Gaussian filtration with respective sigma values. **b**, An integer-label image where the voxel color represents the corresponding Frangi filter scale contributor, as denoted by the border color. **c**, Similarly, an integer-label image where the voxel color represents the corresponding Laplacian of Gaussian (LoG) filter scale contributor, as denoted by the border color.



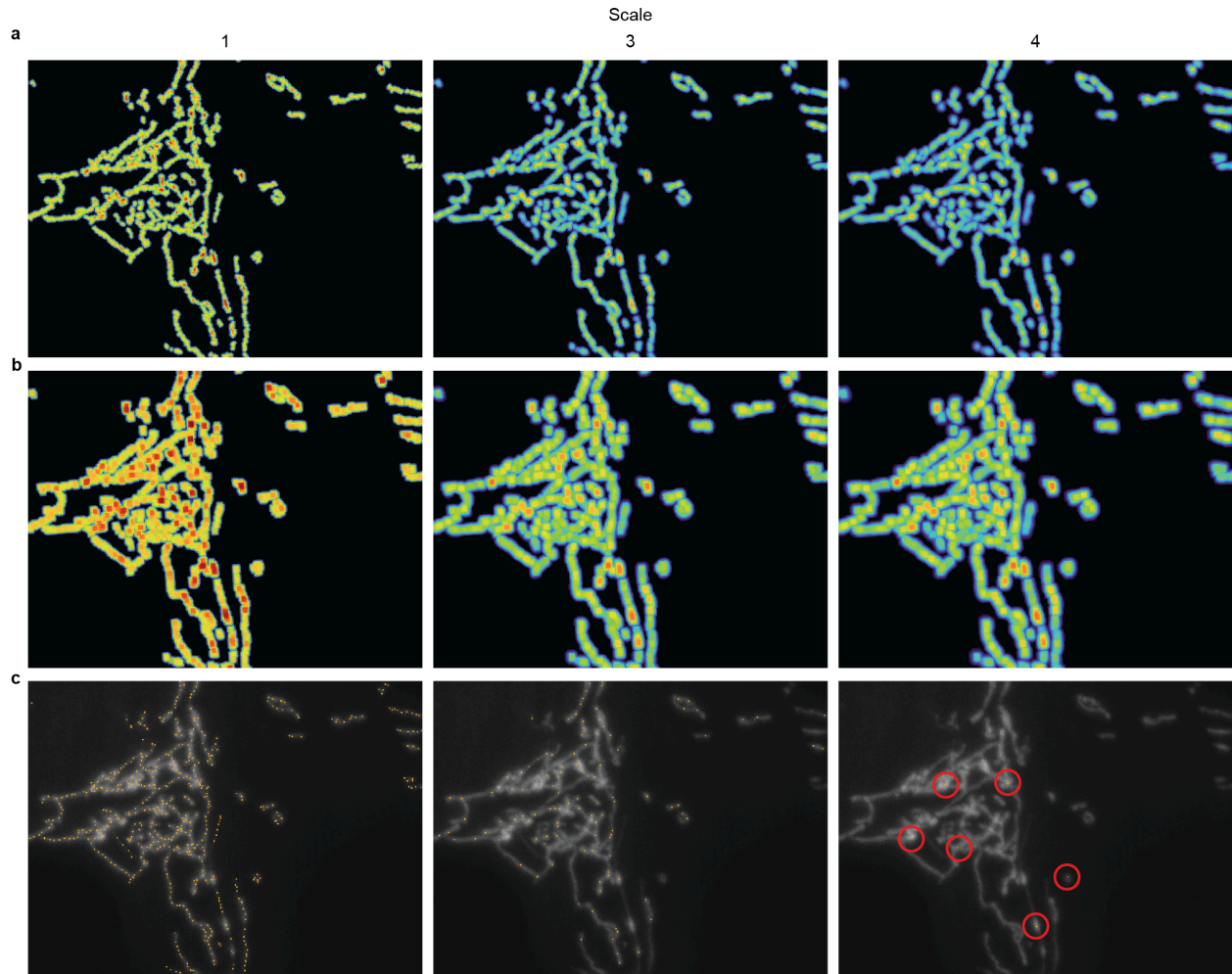
Extended Data Fig. 4: Semantic and instance segmentation

a, A 3D fluorescently mitochondrial-labeled cell is binarized post-structural enhancement filtering. **b**, A small binary opening operation is applied to smooth out irregularities and prune weak single-pixel connections. **c**, The raw fluorescence image is shown with its (**d**) corresponding instance segmented objects.



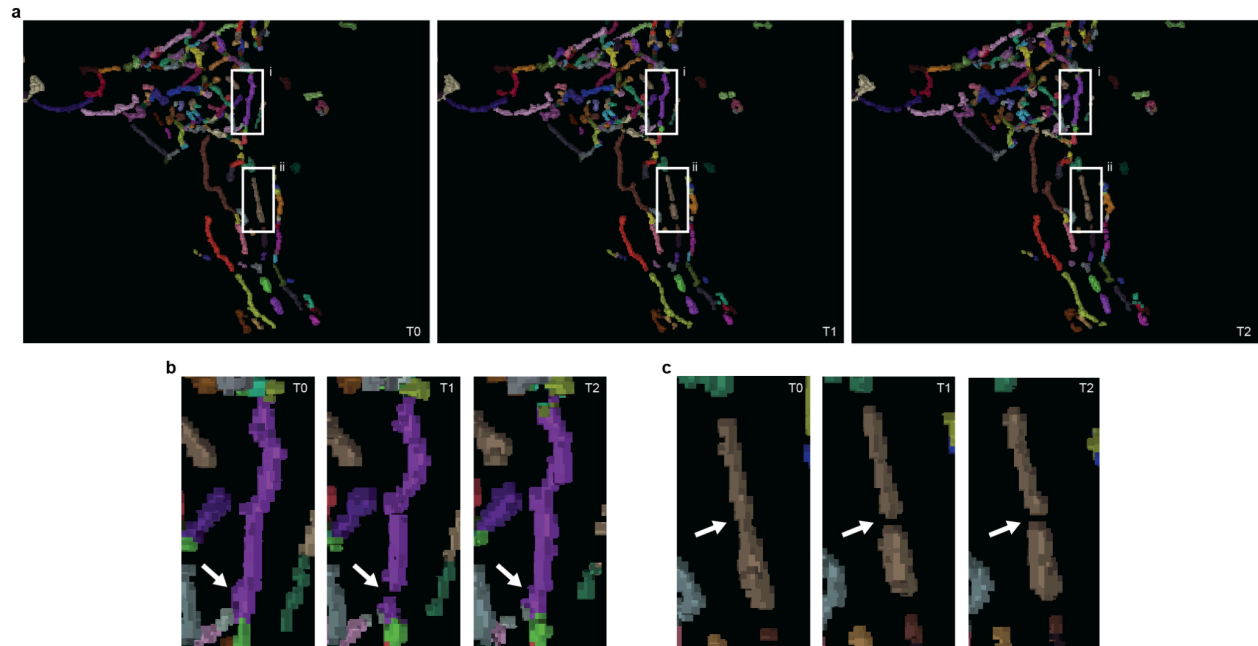
Extended Data Fig. 5: Computationally efficient distance transformation using segmentation border coordinate k-d trees

a, A 2D XY orthogonal slice of a 3D fluorescently mitochondrial-labeled cell from a single object lightsheet microscope (SOLS). **b**, The same 2D slice as in **(a)** of the instance segmentation of the 3D dataset. **c**, The border mask of the instance segmentation of **(b)** superimposed on **(a)**, obtained via a one-voxel binary dilation of the instance segmentation mask, followed by subtraction of the instance segmentation mask. **d**, The same 2D slice as in **(a)** of the distance transformation image acquired by calculating the nearest neighbor distance of the voxel coordinates in **(b)** to the voxel coordinates in **(c)**. **e**, The mean intensity projection of the 3D border mask of the instance segmentation. **f**, The max intensity projection of the 3D distance transformation image of the instance segmentation.



Extended Data Fig. 6: Multi-scale local maxima peak detection for mocap marking

a, A 3D fluorescently mitochondrial-labeled cell's post-processing volume is run through a Laplacian of Gaussian filter at different scales. Shown here is a filter sigma of 0.862, 1.67, and 2.07, (left, middle, right) corresponding to scales 1, 3, and 4, of 5 total scales. **b**, A maximum filter is run across the 4D stack of Laplacian of Gaussian filtered images (**a**). Shown here are again images corresponding to scales 1, 3, and 4, of 5 total scales. **c**, The raw fluorescence intensity image overlaid with single orange voxels corresponding to locations where the intensity value of the Laplacian of Gaussian image (**a**) is equal to the intensity value of the maximum filtered image (**b**) at different scales, again shown at scales 1, 3, and 4, of 5 total scales. Red circles are to indicate the few voxels at scale 4 where voxel intensity values match, indicating fewer (though still important) regions of larger scale structures.



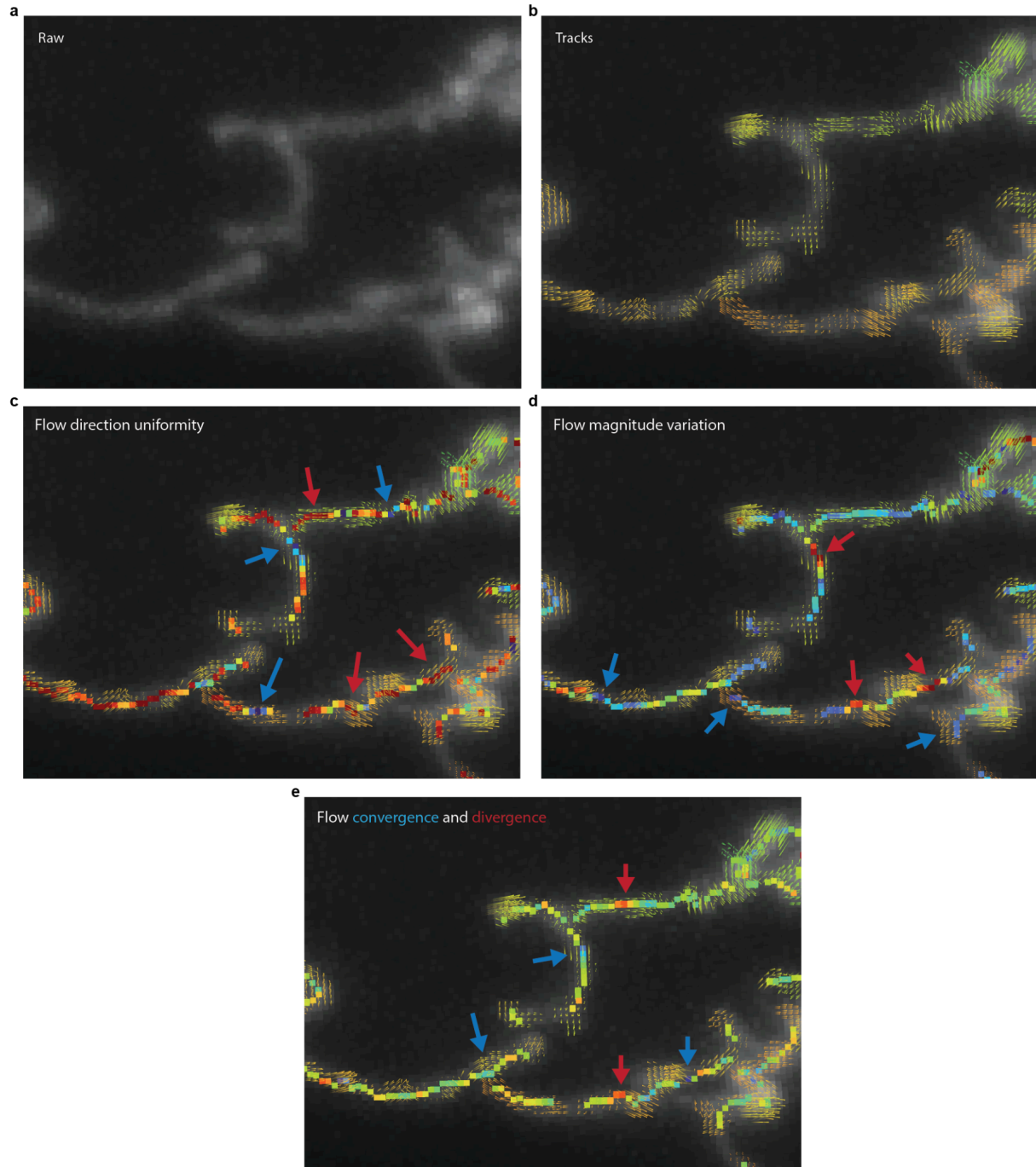
Extended Data Fig. 7: Temporal continuity in organelle tracking via forward and backward interpolation of semantic segmentations across frames

a, Three consecutive frames of labeled semantic segmentations of mitochondrial branch objects after undergoing forward and backward flow interpolation for voxel label reassignment based on T0's object labels. **b**, An example of an object (purple, **a** i.) undergoing a fission event in T1, and fusion event in T2, while keeping track of original T0 labeled voxels, despite the object's connectivity discontinuity between frames. **c**, Another example of an object (brown, **a** ii.) undergoing a fission event in T1, while keeping track of original T0 labeled voxels, despite the object's connectivity discontinuity in T1 and T2.



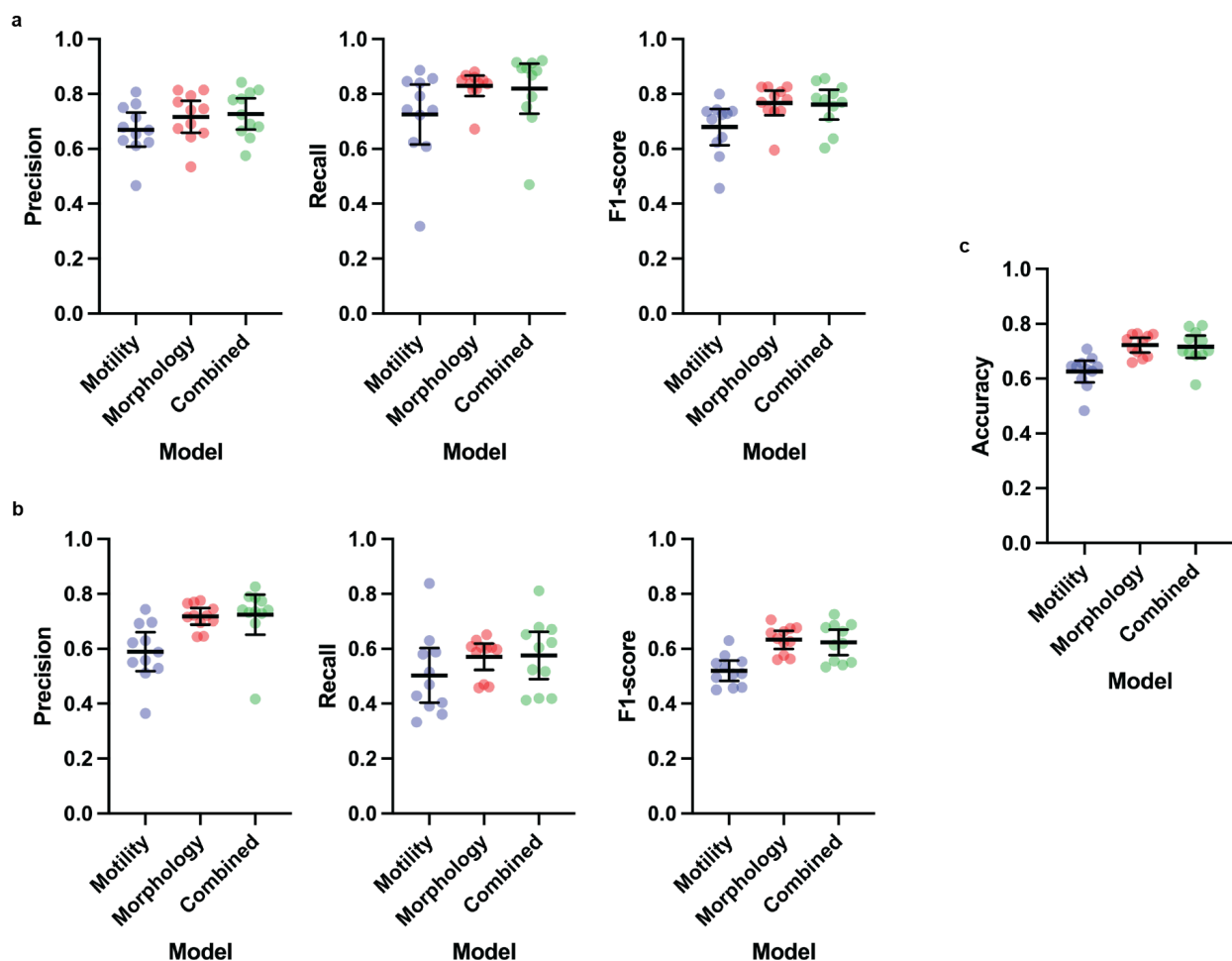
Extended Data Fig. 8: Automated tracking and flow interpolation from iPhone camera video frames and corresponding semantic segmentation masks

a, Four frames at T15, T30, T45, and T60 (left to right) of a 66 frame iPhone video taken at 29.98 fps using an iPhone 12 Pro, with a resolution of 1920x1080 pixels. **b**, The same corresponding frames as **(a)** after segmentation with Meta's Segment Anything model, and selection of semantic segmentations corresponding to the highlighted subject. **c**, The same corresponding frames as **(b)** after running the original video's frames and segmentation mask through Nellie's mocap marking, tracking, and flow interpolation pipelines, generating tracks for 5% of all pixels in the 3D (TYX) mask. **d**, A zoom in portion near a region of relatively abundant movement, the subject's feet, in the corresponding frames of **(c)**. Tracks are colored by frame number, where T0 is dark blue and T66 is dark red based on a 'turbo' colormap, where each track is capped to a 5-frame tail.



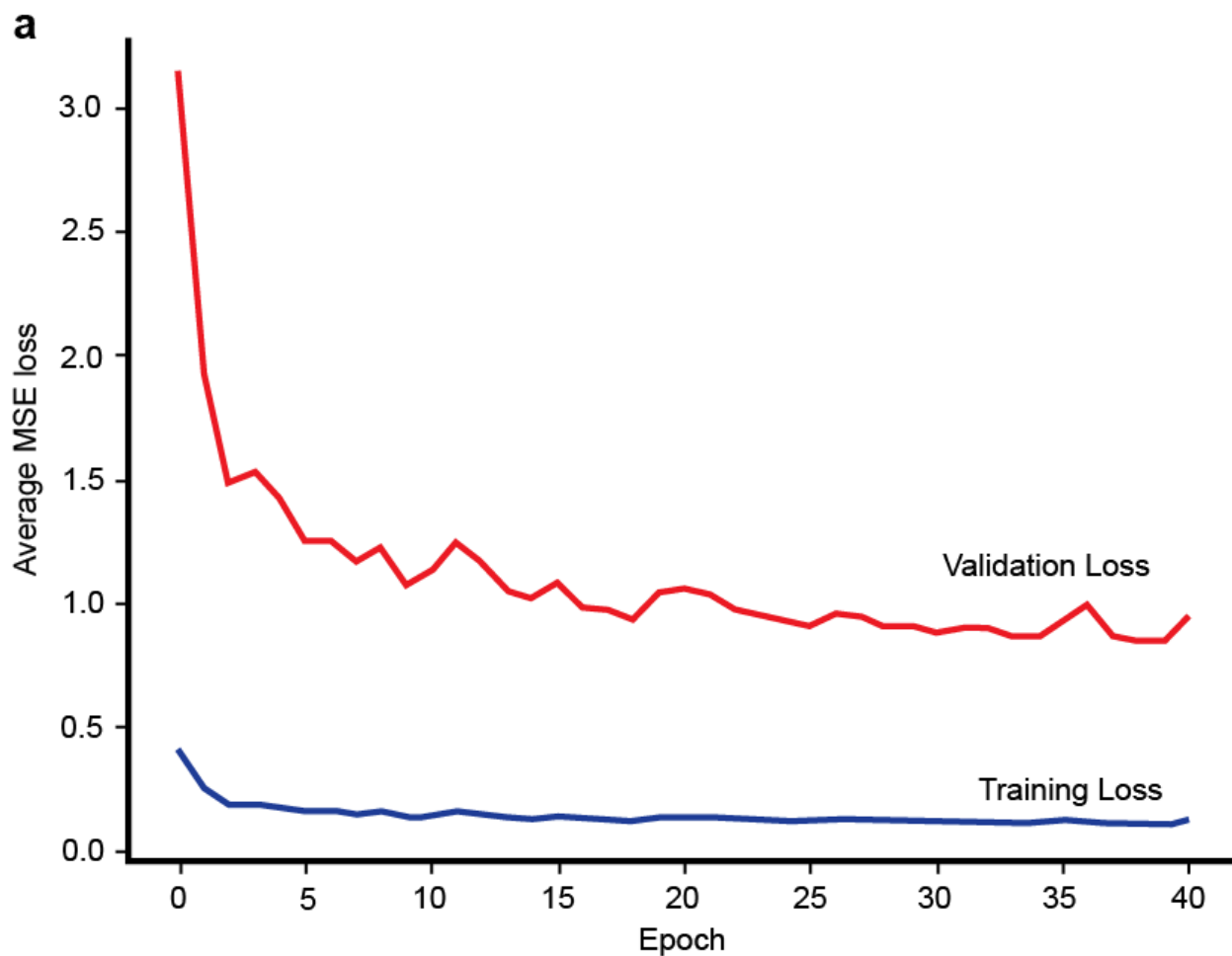
Extended Data Fig. 9: Local skeleton node flow vector feature extraction

a, A close up of a 3D fluorescently mitochondria-labeled cell's raw fluorescence intensity image overlaid with **(b)** its forward-interpolated flow vectors. Voxels of the skeletonized mitochondria semantic segmentation masks are overlaid with the following values: **c**, the uniformity of the skeleton voxel's local flow vectors directions, where red (voxels and arrows) indicates higher directional uniformity, **d**, the standard deviation of the skeleton voxel's local flow vectors magnitudes, where red (voxels and arrows) indicates higher magnitude variability, and **e**, the convergence and divergence of the skeleton voxel's local flow vectors to the skeleton voxel coordinate, where red (voxels and arrows) indicates flow vectors diverging away from the skeleton voxel, and blue (voxels and arrows) indicates flow vectors converging towards the skeleton voxel.



Extended Data Fig. 10: Additional performance metrics from organelle unmixing random forest classifiers

The precision, recall, and F1-score for Golgi (**a**) and mitochondria (**b**) classification of the motility-only, morphology-only and motility and morphology combined random forest models. **c**, The combined accuracy metric of the same three models for overall classification.



Extended Data Fig. 11: Training and validation loss curves for unsupervised training of a GNN autoencoder

a, The training and validation loss curves, based on average MSE loss for the epoch, during training of the unsupervised GNN autoencoder used in the multi-mesh organelle graph latent space comparison case study.

Code availability

The Nellie pipeline and its Napari-based plugin is fully written in Python. The Python code and plugin are freely available online via Github at

<https://github.com/aelefebv/nellie>. Supplemental materials for non pipeline-related code can be found via Github at <https://github.com/aelefebv/nellie-supplemental>.

Contributions

A.E.Y.T.L. conceived of and designed Nellie and its pipeline, wrote the manuscript, created the figures, developed and wrote the code, performed the data analysis, and supervised the study. G.S. and K.H. provided experimental design ideas. A.E.Y.T.L. and G.S. alpha-tested the code, and performed cell-based maintenance and experiments, as well as microscopy experiments. T.Y.L., E.S., and M.P.L. provided cells and reagents. A.E.Y.T.L., G.S., K.H., and B.K.M provided helpful feedback on experimental design, data interpretation, and edited the manuscript.

Acknowledgments

The authors would like to thank Andrew G. York for helpful discussions on the pipeline, Alfred Millett-Sikking's advice and guidance on microscopy with the SOLS, and Evelia Salinas' insights on fluid dynamics and its applications to this pipeline. The authors also thank Brian Feng, Matthew Onsum, and Charlie Ledogar for reviewing the manuscript for its content, and Minna Kane and Colin Sanford for reviewing the manuscript for its wording and grammar. Thank you finally to Calico Life Sciences LLC for supporting this work.

Ethics declarations

The authors declare no competing interests.

References

1. Chen, W., Zhao, H. & Li, Y. Mitochondrial dynamics in health and disease: mechanisms and potential targets. *Signal Transduct. Target. Ther.* **8**, 1–25 (2023).
2. Tilokani, L., Nagashima, S., Paupe, V. & Prudent, J. Mitochondrial dynamics: overview of molecular mechanisms. *Essays Biochem.* **62**, 341–360 (2018).
3. Lewis, S. C., Uchiyama, L. F. & Nunnari, J. ER-mitochondria contacts couple mtDNA synthesis with mitochondrial division in human cells. *Science* **353**, aaf5549 (2016).
4. Lima, T., Li, T. Y., Mottis, A. & Auwerx, J. Pleiotropic effects of mitochondria in aging. *Nat. Aging* **2**, 199–213 (2022).
5. Eisner, V., Picard, M. & Hajnóczky, G. Mitochondrial dynamics in adaptive and maladaptive cellular stress responses. *Nat. Cell Biol.* **20**, 755–765 (2018).
6. Ziegler, D. V., Martin, N. & Bernard, D. Cellular senescence links mitochondria-ER contacts and aging. *Commun. Biol.* **4**, 1–14 (2021).
7. Gottschling, D. E. & Nyström, T. The Upsides and Downsides of Organelle Interconnectivity. *Cell* **169**, 24–34 (2017).
8. Voeltz, G. K., Sawyer, E. M., Hajnóczky, G. & Prinz, W. A. Making the connection: How membrane contact sites have changed our view of organelle biology. *Cell* **187**, 257–270 (2024).
9. Donahue, E. K. F., Ruark, E. M. & Burkewitz, K. Fundamental roles for inter-organelle communication in aging. *Biochem. Soc. Trans.* **50**, 1389–1402 (2022).
10. Lefebvre, A. E. Y. T., Ma, D., Kessenbrock, K., Lawson, D. A. & Digman, M. A. Automated segmentation and tracking of mitochondria in live-cell time-lapse images. *Nat. Methods* **18**, 1091–1102 (2021).
11. Valente, A. J., Maddalena, L. A., Robb, E. L., Moradi, F. & Stuart, J. A. A simple ImageJ macro tool for analyzing mitochondrial network morphology in mammalian cell culture. *Acta Histochem.* **119**, 315–326 (2017).

12. Viana, M. P., Lim, S. & Rafelski, S. M. Quantifying mitochondrial content in living cells. *Methods Cell Biol.* **125**, 77–93 (2015).
13. Kichuk, T. *et al.* Using MitER for 3D analysis of mitochondrial morphology and ER contacts. *Cell Rep. Methods* **4**, (2024).
14. Wang, Z. *et al.* MitoTNT: Mitochondrial Temporal Network Tracking for 4D live-cell fluorescence microscopy data. *PLOS Comput. Biol.* **19**, e1011060 (2023).
15. Kandel, J., Chou, P. & Eckmann, D. M. Automated detection of whole-cell mitochondrial motility and its dependence on cytoarchitectural integrity. *Biotechnol. Bioeng.* **112**, 1395–1405 (2015).
16. Winter, M. R., Fang, C., Banker, G., Roysam, B. & Cohen, A. R. Axonal transport analysis using Multitemporal Association Tracking. *Int. J. Comput. Biol. Drug Des.* **5**, 35–48 (2012).
17. Vallmitjana, A., Civera-Tregon, A., Hoenicka, J., Palau, F. & Benitez, R. Motion estimation of subcellular structures from fluorescence microscopy images. *Conf. Proc. Annu. Int. Conf. IEEE Eng. Med. Biol. Soc. IEEE Eng. Med. Biol. Soc. Annu. Conf.* **2017**, 4419–4422 (2017).
18. Alsina, A. *et al.* Real-time subpixel-accuracy tracking of single mitochondria in neurons reveals heterogeneous mitochondrial motion. *Biochem. Biophys. Res. Commun.* **493**, 776–782 (2017).
19. Miller, K. E., Liu, X.-A. & Puthanveetil, S. V. Automated measurement of fast mitochondrial transport in neurons. *Front. Cell. Neurosci.* **9**, (2015).
20. Yang, Y. *et al.* Label-free tracking of single organelle transportation in cells with nanometer precision using a plasmonic imaging technique. *Small Weinheim. Bergstr. Ger.* **11**, 2878–2884 (2015).
21. Cheezum, M. K., Walker, W. F. & Guilford, W. H. Quantitative Comparison of Algorithms for Tracking Single Fluorescent Particles. *Biophys. J.* **81**, 2378–2388 (2001).
22. Martens, K. J. A., Turkowyd, B., Hohlbein, J. & Endesfelder, U. Temporal analysis of relative distances (TARDIS) is a robust, parameter-free alternative to single-particle tracking. *Nat.*

Methods 1–8 (2024) doi:10.1038/s41592-023-02149-7.

23. Liu, T.-L. *et al.* Observing the cell in its native state: Imaging subcellular dynamics in multicellular organisms. *Science* **360**, eaaq1392 (2018).
24. Basu, H. & Schwarz, T. L. QuoVadoPro, an Autonomous Tool for Measuring Intracellular Dynamics Using Temporal Variance. *Curr. Protoc. Cell Biol.* **87**, e108 (2020).
25. Tinevez, J.-Y. *et al.* TrackMate: An open and extensible platform for single-particle tracking. *Methods* **115**, 80–90 (2017).
26. Boecker, C. A., Olenick, M. A., Gallagher, E. R., Ward, M. E. & Holzbaur, E. L. F. ToolBox: Live Imaging of intracellular organelle transport in induced pluripotent stem cell-derived neurons. *Traffic* **21**, 138–155 (2020).
27. Basu, H., Ding, L., Pekkurnaz, G., Cronin, M. & Schwarz, T. L. Kymolyzer, a Semi-Autonomous Kymography Tool to Analyze Intracellular Motility. *Curr. Protoc. Cell Biol.* **87**, e107 (2020).
28. Chen, J. *et al.* The Allen Cell and Structure Segmenter: a new open source toolkit for segmenting 3D intracellular structures in fluorescence microscopy images. 491035 Preprint at <https://doi.org/10.1101/491035> (2020).
29. Isensee, F., Jaeger, P. F., Kohl, S. A. A., Petersen, J. & Maier-Hein, K. H. nnU-Net: a self-configuring method for deep learning-based biomedical image segmentation. *Nat. Methods* **18**, 203–211 (2021).
30. Fischer, C. A. *et al.* MitoSegNet: Easy-to-use Deep Learning Segmentation for Analyzing Mitochondrial Morphology. *iScience* **23**, 101601 (2020).
31. Lam, R. *et al.* Learning skillful medium-range global weather forecasting. *Science* **382**, 1416–1421 (2023).
32. Frangi, A. F., Niessen, W. J., Vincken, K. L. & Viergever, M. A. Multiscale vessel enhancement filtering. in *Medical Image Computing and Computer-Assisted Intervention — MICCAI'98* (eds. Wells, W. M., Colchester, A. & Delp, S.) 130–137 (Springer, Berlin,

Heidelberg, 1998). doi:10.1007/BFb0056195.

33. Otsu, N. A Threshold Selection Method from Gray-Level Histograms. *IEEE Trans. Syst. Man Cybern.* **9**, 62–66 (1979).
34. Zack, G. W., Rogers, W. E. & Latt, S. A. Automatic measurement of sister chromatid exchange frequency. *J. Histochem. Cytochem.* **25**, 741–753 (1977).
35. Viana, M. Software for Quantifying Mitochondrial Content in Live Cells: vianamp/MitoGraph. (2019).
36. Lee, T. C., Kashyap, R. L. & Chu, C. N. Building Skeleton Models via 3-D Medial Surface Axis Thinning Algorithms. *CVGIP Graph. Models Image Process.* **56**, 462–478 (1994).
37. Meagher, D. Geometric modeling using octree encoding. *Comput. Graph. Image Process.* **19**, 129–147 (1982).
38. Bentley, J. L. Multidimensional binary search trees used for associative searching. *Commun. ACM* **18**, 509–517 (1975).
39. Borgefors, G. Distance transformations in arbitrary dimensions. *Comput. Vis. Graph. Image Process.* **27**, 321–345 (1984).
40. Hu, M.-K. Visual pattern recognition by moment invariants. *IRE Trans. Inf. Theory* **8**, 179–187 (1962).
41. Kirillov, A. *et al.* Segment Anything. Preprint at <https://doi.org/10.48550/arXiv.2304.02643> (2023).
42. Ho, T. K. Random decision forests. in *Proceedings of 3rd International Conference on Document Analysis and Recognition* vol. 1 278–282 vol.1 (1995).
43. Kipf, T. N. & Welling, M. Variational Graph Auto-Encoders. Preprint at <https://doi.org/10.48550/arXiv.1611.07308> (2016).
44. Elfving, S., Uchibe, E. & Doya, K. Sigmoid-Weighted Linear Units for Neural Network Function Approximation in Reinforcement Learning. Preprint at <https://doi.org/10.48550/arXiv.1702.03118> (2017).

45. Micheli, A. Neural Network for Graphs: A Contextual Constructive Approach. *IEEE Trans. Neural Netw.* **20**, 498–511 (2009).
46. Scarselli, F., Gori, M., Tsoi, A. C., Hagenbuchner, M. & Monfardini, G. The Graph Neural Network Model. *IEEE Trans. Neural Netw.* **20**, 61–80 (2009).
47. Veličković, P. *et al.* Graph Attention Networks. Preprint at <https://doi.org/10.48550/arXiv.1710.10903> (2018).
48. Chakrabarti, R. *et al.* INF2-mediated actin polymerization at the ER stimulates mitochondrial calcium uptake, inner membrane constriction, and division. *J. Cell Biol.* **217**, 251–268 (2017).
49. Kingma, D. P. & Ba, J. Adam: A Method for Stochastic Optimization. Preprint at <https://doi.org/10.48550/arXiv.1412.6980> (2017).
50. Maaten, L. van der & Hinton, G. Visualizing Data using t-SNE. *J. Mach. Learn. Res.* **9**, 2579–2605 (2008).
51. Ahlers, J. *et al.* napari: a multi-dimensional image viewer for Python. Zenodo <https://doi.org/10.5281/zenodo.8115575> (2023).
52. Bray, M.-A. *et al.* Cell Painting, a high-content image-based assay for morphological profiling using multiplexed fluorescent dyes. *Nat. Protoc.* **11**, 1757–1774 (2016).
53. Millett-Sikking, A. & York, A. High NA single-objective light-sheet. (2019).
54. Paszke, A. *et al.* PyTorch: An Imperative Style, High-Performance Deep Learning Library. Preprint at <https://doi.org/10.48550/arXiv.1912.01703> (2019).
55. Fey, M. & Lenssen, J. E. Fast Graph Representation Learning with PyTorch Geometric. Preprint at <https://doi.org/10.48550/arXiv.1903.02428> (2019).